

Mechanistic Logic Underlying the Axonal Transport of Cytosolic Proteins

David A. Scott,^{1,2} Utpal Das,^{1,2} Yong Tang,¹ and Subhojit Roy^{1,*}

¹Department of Neurosciences, University of California, San Diego, 312 MTF, 9500 Gilman Drive, MC 0624, La Jolla, CA 92093, USA

²These authors contributed equally to this work

*Correspondence: s1roy@ucsd.edu

DOI 10.1016/j.neuron.2011.03.022

SUMMARY

Proteins vital to presynaptic function are synthesized in the neuronal perikarya and delivered into synapses via two modes of axonal transport. While membrane-anchoring proteins are conveyed in fast axonal transport via motor-driven vesicles, cytosolic proteins travel in slow axonal transport via mechanisms that are poorly understood. We found that in cultured axons, populations of cytosolic proteins tagged to photoactivatable GFP (PAGFP) move with a slow motor-dependent anterograde bias distinct from both vesicular trafficking and diffusion of untagged PAGFP. The overall bias is likely generated by an intricate particle kinetics involving transient assembly and short-range vectorial spurts. In vivo biochemical studies reveal that cytosolic proteins are organized into higher order structures within axon-enriched fractions that are largely segregated from vesicles. Data-driven biophysical modeling best predicts a scenario where soluble molecules dynamically assemble into mobile supra-molecular structures. We propose a model where cytosolic proteins are transported by dynamically assembling into multiprotein complexes that are directly/indirectly conveyed by motors.

INTRODUCTION

The vast majority of the proteins in a neuron are synthesized in cell-bodies and conveyed into axons and presynapses via axonal transport. Distal presynaptic boutons are critically dependent on axonal transport throughout life and functional organization of the adult neuronal circuitry relies upon continued protein synthesis and transport (Kleim et al., 2003). Previous pulse-chase radiolabeling studies have shown that newly synthesized proteins are conveyed via two distinct modes of transport. While proteins with membrane-spanning or anchoring domains are packaged into vesicles and conveyed via fast axonal transport at overall rates of 50–400 mm/day (0.5–4 $\mu\text{m/s}$), cytosolic proteins lacking such domains are transported much more slowly in a transport group historically called Slow Component b (SCb) at rates of 1–10 mm/day (0.01–0.1 $\mu\text{m/s}$) (reviewed in Brown, 2003 and Roy et al., 2005).

Of the 200+ cytosolic proteins that are conveyed in slow axonal transport, many are enriched at presynaptic terminals as shown by detailed radiolabeling studies (Garner and Mahler, 1987). Similar studies have also characterized the transport of two well-known presynaptic proteins—synapsin and calcium/calmodulin-dependent kinase (CamKIIa)—showing that after perikaryal synthesis, the vast majority of these synaptic proteins move with slow overall rates, whereas a smaller fraction ($\approx 15\%$) is conveyed rapidly in fast axonal transport (Baitinger and Willard, 1987; Garner and Lasek, 1982; Lasek et al., 1984; Lund and McQuarrie, 2001, 2002; Paggi and Petrucci, 1992; Petrucci et al., 1991).

By their very nature, pulse-chase radiolabeling experiments offer a descriptive and indirect view of axonal transport and provide little insight into the mechanisms that generate this motion. Thus, though the overall transport of these synaptic proteins was described decades ago, critical questions remain unanswered. How do inherently soluble proteins move in this slow sustained manner? What is the underlying molecular basis of this movement? What (if any) is the role of diffusion in this process? What is the nature of the minor pool that is conveyed in fast axonal transport? To date, no evidence-based model can provide molecular details that can adequately explain the slow sustained transit of soluble proteins seen in the classic radiolabeling studies decades ago.

To address these questions we developed an assay for cytosolic cargo transport in cultured neurons by using photoactivatable vectors, in which we could visualize bulk cargo movement and particle dynamics with high resolution. Coupled with in vivo biochemical assays and data-driven biophysical modeling, we show that cytosolic synaptic proteins employ atypical transport strategies. These studies provide evidence for a detailed model that can explain the mechanistic logic behind the axonal transport of these cytosolic cargoes in neurons, providing insights into a long-standing scientific question.

RESULTS

Polarized Bulk Transport of Cytosolic Proteins in Axons

To investigate bulk axonal transport of cytosolic protein populations, we transfected cultured hippocampal neurons with synapsin (synapsin-Ia) or CamKIIa tagged to photoactivatable green fluorescent protein (PAGFP), selectively photoactivated discrete protein pools within the primary axon emerging from the soma (away from presynaptic boutons), and tracked the mobility of photoactivated cytosolic protein populations at various time compressions (Figures 1 and 2). We focused our studies on

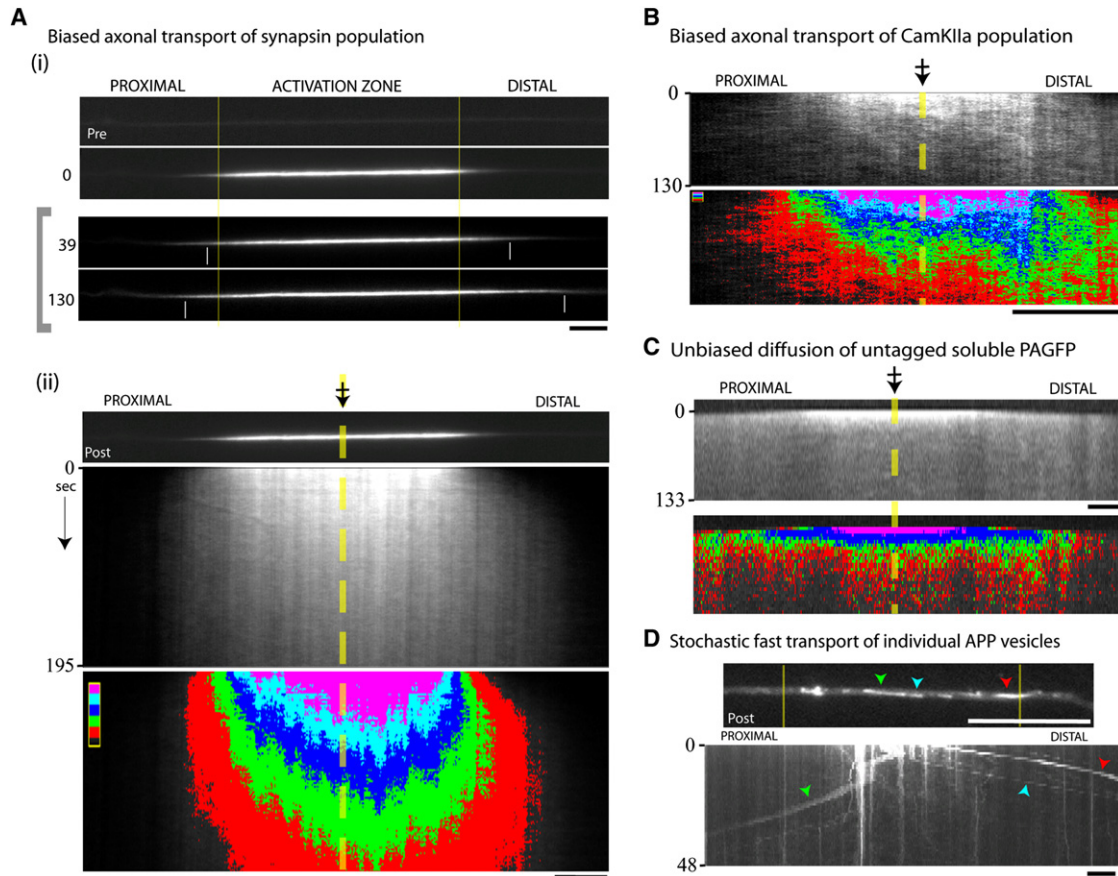


Figure 1. Axonal Transport Dynamics of Cytosolic Proteins

(A) Neurons were cotransfected with PAGFP:synapsin (and soluble mRFP to identify transfected axons); a discrete region within the primary axon was photoactivated, and mobility of the photoactivated protein pool was tracked in living axons by time-lapse imaging.

(i) Top: Representative example showing a transfected axon pre- and postactivation. The vertical yellow bars denote the boundaries of the photoactivated zone throughout the frames. Bottom: Selected frames from the time-lapse showing the anterograde migration of the photoactivated plume of fluorescence (time in s, left). The small white vertical bars within the images mark the approximate position of the wave fronts. Note that the frames within the gray bracket (left) were linearly scaled to maximize the bit depth within each image and highlight the leading edges of the fluorescent wave fronts.

(ii) Kymograph from the time-lapse frame above (dashed yellow line and crossed arrow depicts center of the photoactivated zone). In the lower panel, the grayscale values of the kymograph above were assigned five pseudocolored intensity bins (red: lowest intensity bin, pink: highest intensity bin above background), allowing clear visualization of the anterograde bias of the fluorescent plume.

(B) A similar biased transit was seen for the cytosolic protein CamKIIa as shown in these representative images.

(C) The movement of untagged PAGFP was rapid, bidirectional, and unbiased.

(D) By using a similar photoactivation paradigm PAGFP:APP vesicles stochastically departed the fluorescent pool over time. Green, blue, and red arrowheads mark the position of individual photoactivated vesicles in the postactivation image (above) and the kymograph (below). Scale bars = 5 μ m. Elapsed time in seconds is shown on the left side of the kymograph.

two cytosolic proteins enriched at synapses—synapsin and CamKIIa—as radiolabeling studies have established the overall transport of these proteins, showing that they are largely conveyed by slow axonal transport (Baitinger and Willard, 1987; Lund and McQuarrie, 2001, 2002; Petrucci et al., 1991). The GFP fusions of these synaptic proteins have been characterized in previous studies (Gitler et al., 2004; Sturgill et al., 2009; also see Figure S1, available online). Note that punctate particles are clearly visible both in axons expressing the fluorescent proteins and adjacent naive axons (Figure S1B) suggesting that the fusion proteins generally mimic the behaviors of their in situ counterparts. Figures 1A and 1B show typical results

from photoactivation experiments (also see Movies S1 and S2, available online).

The photoactivated axonal protein pool of synapsin and CamKIIa dispersed as a plume of fluorescence with a distinct anterograde bias, as shown in the representative kymographs (Figures 1A and 1B). This directional bias of fluorescence is unlikely to be a result of some nonspecific bulk axonal flow that moves all soluble proteins in its wake, as there was no bias in the axonal dispersion of untagged PAGFP, which showed bidirectional rapid diffusion as expected (Figure 1C; also see Movies S3 and S5). Also, the intensity-center analyses (see below) are not likely influenced by photo-bleaching as similar trends of intensity-center shifts were

observed under imaging conditions that greatly minimized photobleaching (Figures S2A and S2B). The transport behavior of cytosolic proteins is also very different from the fast component amyloid precursor protein (APP), where discrete photoactivated vesicles rapidly escaped the activated zone over time (Figure 1D; also see Movie S4), in line with conventional stochastic motor-driven transport (Kaether et al., 2000). Similar results were also obtained with PAGFP:synaptophysin (data not shown).

Biased Axonal Transport of Cytosolic Cargoes at Expected Overall Rates

If the biased anterograde migration of the synapsin and CamKIIa population in our studies is the visual correlate of the slow axonal transport seen in pulse-chase radiolabeling studies, the overall vectorial bias of the fluorescence pool in our experiments should be similar to the overall rates of the radiolabeled population. To address this we quantified the bulk movement of the entire photoactivated pool by using intensity-center shift analysis (Figure 2A). Briefly, the intensity center in a given frame is a quantitative center of the distribution of binned fluorescence intensities along a line scan within the photoactivated zone. A bulk vectorial movement of fluorescent molecules within the axon would lead to a corresponding shift in the intensity center as well. Anterograde shifts were consistently seen in the photoactivated pools of both synapsin and CamKIIa though there were differences in the overall kinetics as shown in Figure 2B. Specifically, for CamKIIa, there was a slight lag in the initiation of intensity-center shift as well as a periodic variation that was more pronounced than that for synapsin. Note that there is an expected flattening of the wave after the initial rise as the fluorescent molecules leave the analyzed area (photoactivated zone) over time.

Despite these differences in the overall nature of the intensity-center shifts between synapsin and CamKIIa, there were similarities in their initial intensity shifts, suggesting possible commonalities between mechanisms transporting these cytosolic proteins—a notion supported by radiolabeling studies as well (Garner and Lasek, 1982). To investigate this in more detail we focused on the initial intensity shift, imaging the activated zone with higher time compression. Indeed there was some similarity in the overall transport behaviors of both proteins (Figure 2B, lower panel). Linear regression slopes were 0.008 and 0.01 respectively, equivalent to predicted average rates of 0.008–0.01 $\mu\text{m/s}$ for the entire population. These data are comparable to known slow rates of synapsin and CamKIIa from *in vivo* radiolabeling experiments, ≈ 0.01 – $0.03 \mu\text{m/s}$ (Baitinger and Willard, 1987; Lund and McQuarrie, 2001; Petrucci et al., 1991), providing confidence in the validity of this assay in evaluating axonal transport of these cytosolic cargoes. Note that similar analysis of untagged soluble PAGFP diffusion does not show any bias in its mobility (Figure 2B, lower right panel).

The Anterograde Bias of Cytosolic Cargoes Is Microtubule and Motor Dependent

The anterogradely biased transit of synapsin and CamKIIa, distinct from the bidirectional unbiased movement of untagged soluble PAGFP in axons, suggests that the movement is not a simple diffusive process. We further tested this notion by analyzing synapsin and CamKIIa transport in the presence of

micromolar amounts of the alkylating agent N-ethyl maleimide (NEM), a known inhibitor of kinesins, dyneins, and myosins (Pfister et al., 1989). Most recently, NEM was used to inhibit molecular motors to dissect their role in mobilizing vesicles at synapses (Shakiryanova et al., 2005), and when perfused in squid axons, 1 μM NEM inhibits bidirectional vesicular transport within minutes (Pfister et al., 1989). This transport inhibition is due to the action of alkylating sulfhydryl groups on motors that profoundly alters their interactions with ATP and microtubules, stalling vesicle-motor complexes (Pfister et al., 1989). Without knowledge of the specific anterograde and retrograde motor(s) moving the assortment of cytosolic proteins, NEM provides a useful tool to examine the role of molecular motors in generating the intensity-center shift of synapsin and CamKIIa in our imaging experiments.

Upon the addition of 0.5 μM NEM, axonal transport of APP vesicles was gradually perturbed and vesicular transport completely ceased at 20 min (Figure 3A). Accordingly, for our experiments we visualized synapsin and CamKIIa transport after 10 min of NEM treatment. We found that such NEM treatment resulted in the accumulation of stationary puncta within axons with a dramatic inhibition of the anterogradely biased motion (Figure 3B). NEM treatment did not lead to any discernible changes in the diffusion kinetics of untagged PAGFP (Figures S2C and S2D). Addition of nocodazole, a microtubule-depolymerizing agent, also resulted in an inhibition of the anterograde bias (Figure 3C and Figure S3A) as did the cellular metabolic poison (oxidative phosphorylation uncoupler) 2,4-dinitrophenol (2,4-DNP) (Figure S3B). Finally, coexpression of headless kinesins 1A, 1B, and 1C (also called Kif-5A, Kif-5B, and Kif-5C) known to act in a dominant negative fashion to inhibit kinesin-1 mediated transport (Kozielski et al., 1997; Uchida et al., 2009) also inhibited the anterograde bias of synapsin (Figure S3C), further suggesting that the bias is dependent on the activity of motors.

Intricate Particle Kinetics Underlie the Slow Transport of Cytosolic Proteins

The above experiments show that populations of synapsin and CamKIIa move along axons with a motor-dependent anterograde bias. This movement seems different from fast transport, where individual vesicles are stochastically transported by molecular motors. What is the underlying molecular basis for this unconventional motion of cytosolic protein populations? We reasoned that the overall biased transit of these proteins is ultimately mediated by the movement of particles that are transport competent. First, when neurons are stained for endogenous cytosolic synaptic proteins, particulate structures are seen within naive axons (Figure S1A, and also see Fletcher et al., 1991; Roy et al., 2007; Withers et al., 1997), suggesting that these are the native structural form of cytosolic proteins within axons. Second, particulate structures are also clearly present within photoactivated zones in our experiments (note vertical lines in kymographs, Figure 1A and elsewhere). Third, when the anterograde bias of the photoactivated pool was inhibited with NEM or nocodazole, stalled particles are seen in axons (Figure 3B and Figure S3A). Furthermore, upon carefully examining kymographs, we could occasionally pick out diagonal tracks

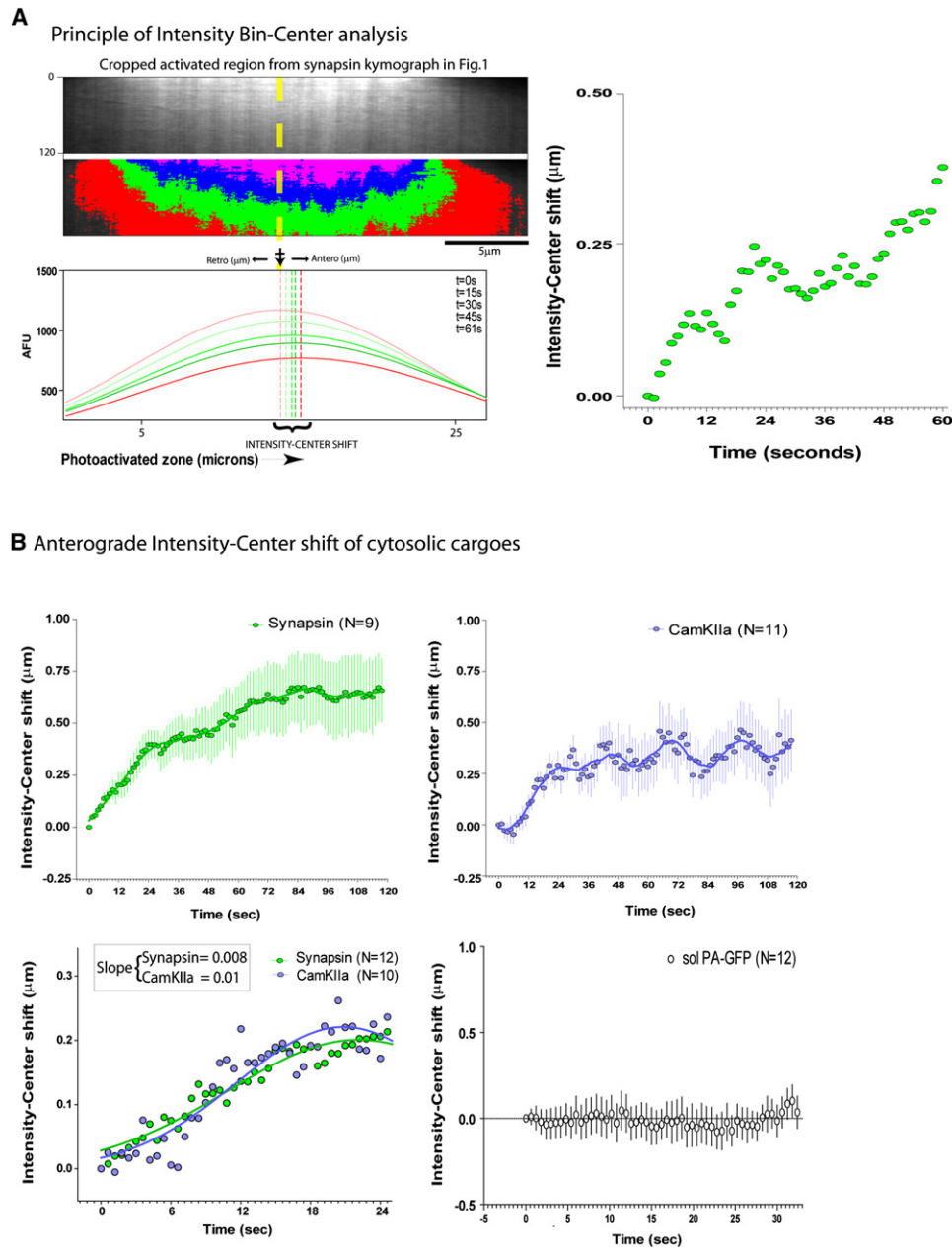


Figure 2. Quantitative Strategy to Analyze the Bulk Movement of Photoactivated Protein Pools

(A) Top panels show cropped kymographs from the photoactivated zone in Figure 1. Each curve below represents average-intensity bins along a line scan within the photoactivated axonal segment for a given frame (time, upper right key; Gaussian fits are shown). Dashed vertical lines represent the position of the peak value for each intensity curve (intensity center). Note that there is a left to right (anterograde) shift in the positions of the peaks over time (intensity-center shift). The graph on the right is a plot of the intensity-center shift over time. Scale bar: lower right.

(B) Quantitative data from multiple synapsin and CamKIIa experiments (mean \pm SEM) showing anterograde intensity-center shifts for both protein populations. In the bottom panels the first few seconds after photoactivation was imaged with higher time compressions (Gaussian fits are shown). Predicted average rates of the overall synapsin and CamKIIa population in these experiments (derived from linear regression slopes) are comparable to known overall rates of synapsin and CamKIIa seen in previous radiolabeling studies (see text). No shifts are seen with untagged PAGFP (bottom right, mean \pm SEM). Each X axis tick represents an image-acquisition time point in all graphs. Elapsed time in seconds is shown on the left side of the kymograph.

suggestive of vectorial particle motion (see kymographs in Figure 1, for example).

However, our experiments designed to visualize bulk axonal transport of soluble proteins by maximally photoactivating

synapsin and CamKIIa protein pools were not ideal for detecting the movement of individual particles. Accordingly, we photoactivated smaller protein pools, reasoning that stochastic incorporation of fluorescent molecules on synapsin and CamKIIa

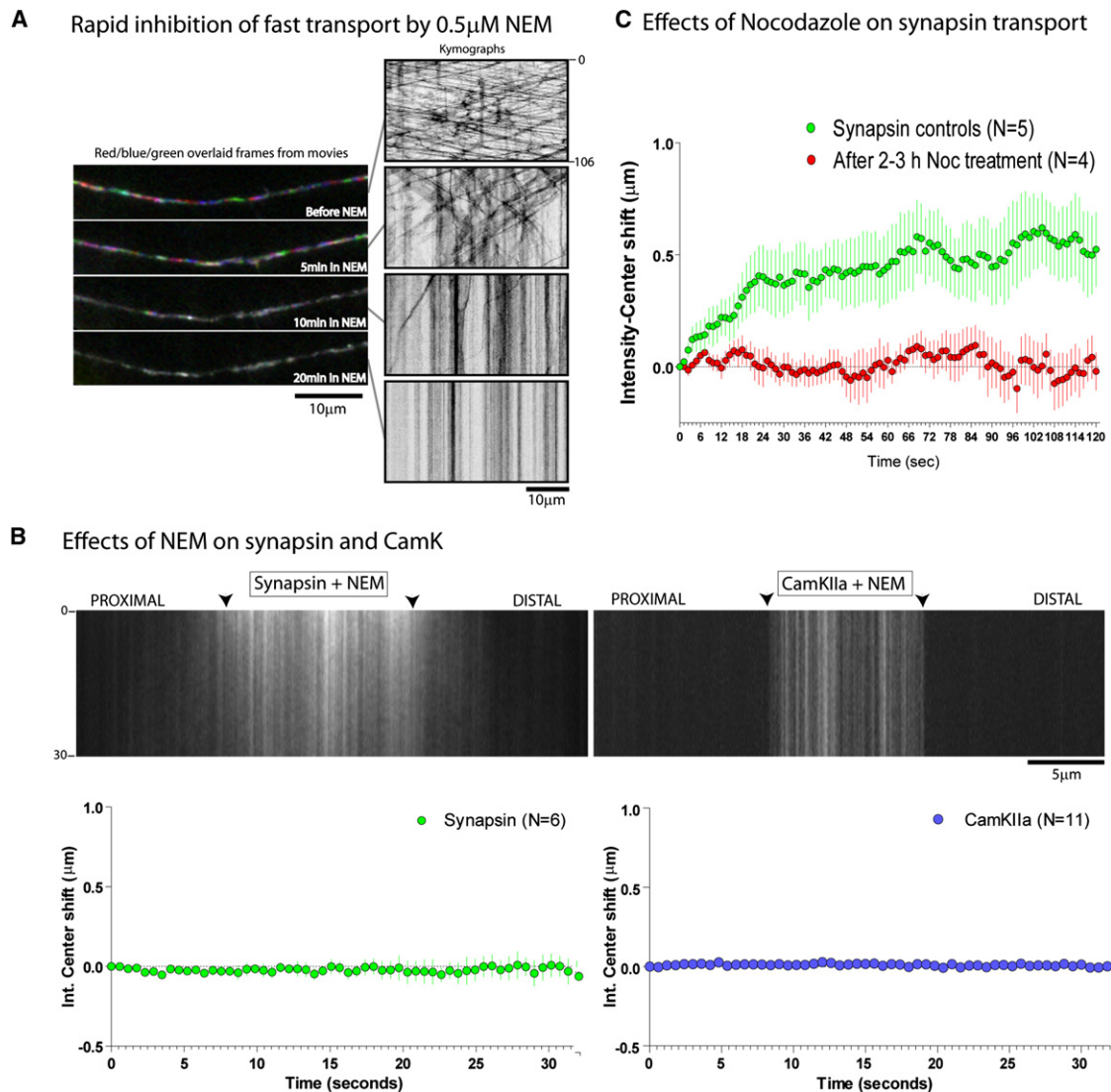


Figure 3. Biased Transport of Cytosolic Cargoes Is Distinct from Untagged PAGFP and Is Motor Dependent

(A) To determine the effects of NEM on generic motor-driven transport, neurons were transfected with APP:YFP and transport of APP vesicles was determined before and after adding 0.5 μ M NEM. Each panel on the left is created by overlapping three consecutive time-lapse frames that were pseudocolored red, blue, and green respectively, before (top frame) and at incremental time points after adding NEM. Corresponding kymographs from the movies are shown on the right. Note that the robust bidirectional vesicular transport was gradually inhibited with NEM treatment.

(B) Neurons transfected with PAGFP:synapsin or PAGFP:CamKIIa were incubated with 0.5 mM NEM for 10 min and photoactivation experiments were performed as described in text. As shown in the representative kymographs (top), NEM treatment greatly inhibited the overall mobility of the photoactivated pool, which led to stalled fluorescent particles within axons and essentially eliminated the anterograde bias, as shown in the graphs below (mean \pm SEM). Scale bars in panels (A) and (B) are on the lower right. Elapsed time in seconds is shown on the right and left of the kymograph.

(C) A similar inhibition of the anterograde bias of synapsin was seen upon treatment of neurons with the microtubule-depolymerizing drug nocodazole (mean \pm SEM, $p < 0.0001$, paired t test).

particles would allow us to see their movement, adopting methods from the speckle microscopy field (Dorn et al., 2008). Indeed, such methods revealed numerous mobile particles within the photoactivated zone as shown in the kymograph examples in Figure S4. These movements were surprisingly intricate, consisting of rapid assembly and disassembly and vectorial spurts of the speckles. Manual analyses of a subset of vectorial tracks from the kymographs show that the average velocities of synapsin and CamKIIa

speckles are comparable to known rates of kinesins and dyneins ($1.981 \pm 0.14 \mu\text{m/s}$ and $1.931 \pm 0.13 \mu\text{m/s}$, mean \pm SEM for anterogradely moving synapsin and CamKIIa, respectively, $n \approx 60$).

Bimodal Axonal Transport of Synapsin

Previous radiolabeling studies have shown that small fractions ($\approx 15\%$) of somatically synthesized cytosolic synaptic proteins are conveyed in fast axonal transport (Baitinger and Willard, 1987;

Paggi and Petrucci, 1992; Petrucci et al., 1991). These data have always been puzzling and the nature of this smaller, rapidly transported pool is poorly understood. To more closely simulate the radiolabeling paradigm, we photoactivated perikaryal PAGFP:synapsin and immediately thereafter imaged the emanating axon to track the migration of the photoactivated protein population from the soma into the axon (Figure 4A; also see Movie S6). We reasoned that such experiments would photoactivate large protein pools and allow us to visualize both the slowly transported wave and the potential persistent particles as they emerged into an axon devoid of background fluorescence.

Focusing on the proximal axonal region (Figure 4A, region of interest [ROI]-A) we saw a gradual migration of synapsin into the axon over time at rates closely resembling slow axonal transport (Figure 4Ai, representative of four such experiments), probably representing the slow transport of synapsin from the perikarya into axons. Next, after the slow-moving front had entered the axon, we imaged the advancing synapsin wave front within ROI-A at higher time compressions (Figure 4Aii). Surprisingly, we saw numerous particles emerge from the leading edge of the wave and move rapidly and persistently along the axon (Figure 4Aii). Such persistent, anterogradely moving particles were also readily visible when we imaged a more distal region of the same axon (Figure 4Aiii, kymograph from ROI-B). Note that the persistently mobile particles in the distal axon originated in the cell body as only the soma was photoactivated in these experiments. Imaging of the fast axonal transport protein APP by using a similar experimental strategy gave entirely different results, in which a deluge of photoactivated APP vesicles rapidly entered the axon a few seconds after perikarya photoactivation as expected (Figure S5; representative of four such experiments, also see Movie S7) and no slowly migrating wave was observed, as seen with synapsin. To determine if the persistent synapsin particles seen in the above experiments were associated with vesicular cargoes moving in fast axonal transport, we cotransfected neurons with GFP:synapsin-I (labeling all synapsin at steady state) and synaptophysin:monomeric red fluorescent protein (mRFP; transmembrane protein moving in fast transport) and simultaneously imaged both cargoes in thin distal axons by using dual-camera imaging (DC2 Dual-Cam system, Photometrics, Tucson, AZ). We found that a large fraction of persistent synapsin particles were colocalized with synaptophysin as shown in Figure 4B. Collectively the data show that while a large population of synapsin moves as a slowly migrating wave (likely with intricate particle kinetics), a subpopulation of somatically derived synapsin associates with vesicles conveying other fast synaptic proteins and moves persistently. These data help reconcile the seemingly conflicting observations by live imaging that synapsin particles clearly move rapidly as transport packets (Ahmari et al., 2000) and the fact that radiolabeling studies have established that the majority of synapsin is conveyed in slow axonal transport (Baitinger and Willard, 1987; Petrucci et al., 1991).

Evidence that Cytosolic Proteins Exist as Proteinaceous Complexes in Brains

The data above support a model where the majority of the cytosolic protein population organizes into particles that undergo

slow transport via intricate kinetics. Particles are invariably seen upon immunostaining of cytosolic proteins in neurons and (at least a fraction of them) probably represent the cargo structure moving in slow transport. What is the nature of these punctate structures and how are they being transported? One possibility is that they represent the association of synapsin and CamKIIa molecules with a proteinaceous particle or macromolecular complex that is transported by motors (Lasek et al., 1984). Another possibility is that these puncta represent the association of individual monomers with vesicles. Indeed, association of both synapsin and CamK with synaptic vesicles is well established (Takamori et al., 2006) and it is possible that they have transient vesicular associations in nonsynaptic compartments as well.

To address the biochemical nature of synapsin and CamKII cargoes in mouse brains *in vivo* we first used classical assays to isolate synaptosomal-rich and synaptosomal-depleted fractions (P2 and S2 respectively, see strategy in Figure 5A). We reasoned that the S2 fractions, largely free from the pre- and postsynaptic terminals (Dunkley et al., 2008; Whittaker, 1993), would probably contain the putative cargo elements transporting these proteins and characterized the nature of synapsin and CamKIIa in these fractions. For these experiments, 4-week-old mouse brains were homogenized under conditions that aim to preserve native interactions and separated into various soluble (S) and pellet (P) fractions (see [Experimental Procedures](#) for further details). If the entire synapsin and CamKII population was completely soluble in nonsynaptic S2 fractions, one would expect that these proteins would exclusively migrate in the supernatant (S₁₀₀) fractions. In line with that, we found that the small signaling molecule RhoGDI, previously used as a soluble marker in neurons (Kimura et al., 2005), is predominantly enriched in the S₁₀₀ fractions (Figure 5A, bottom). Though the axonal transport of signaling molecules has not been rigorously evaluated by radiolabeling, it is generally believed that their intracellular motion is largely diffusive (Brangwynne et al., 2008; Lillemeier et al., 2001; Zeng et al., 2001). However, we found significant amounts of both synapsin and CamKII in the P₁₀₀ pellet fractions (Figure 5A, bottom, see fractions within red box), indicating that fractions of these proteins *in vivo* exist in a state that is not entirely soluble.

As vesicles are also present in the P₁₀₀ fractions, we next asked if synapsin and CamKII are associated with vesicles in these fractions. To determine this we subjected the pellet fractions to sucrose-gradient floatation assays and probed them for synapsin and CamKII, as well as classic transmembrane proteins APP and synaptophysin and a peripherally associated membrane protein (GAP43), all of which are conveyed in fast axonal transport. We found that while all vesicular proteins floated in lighter fractions (as expected), significant quantities of both synapsin and CamKII were present in the high-density fractions that were largely distinct (but partially overlapping) from the transmembrane proteins (Figure 5B, top). Also, while detergent treatments disrupted the vesicular proteins, they had little effect on the higher density fractions of the two cytosolic proteins (Figure 5B, bottom and Figure S6A). The separation of membranous and cytosolic proteins was also observed in density gradients from axon-enriched corpus callosum

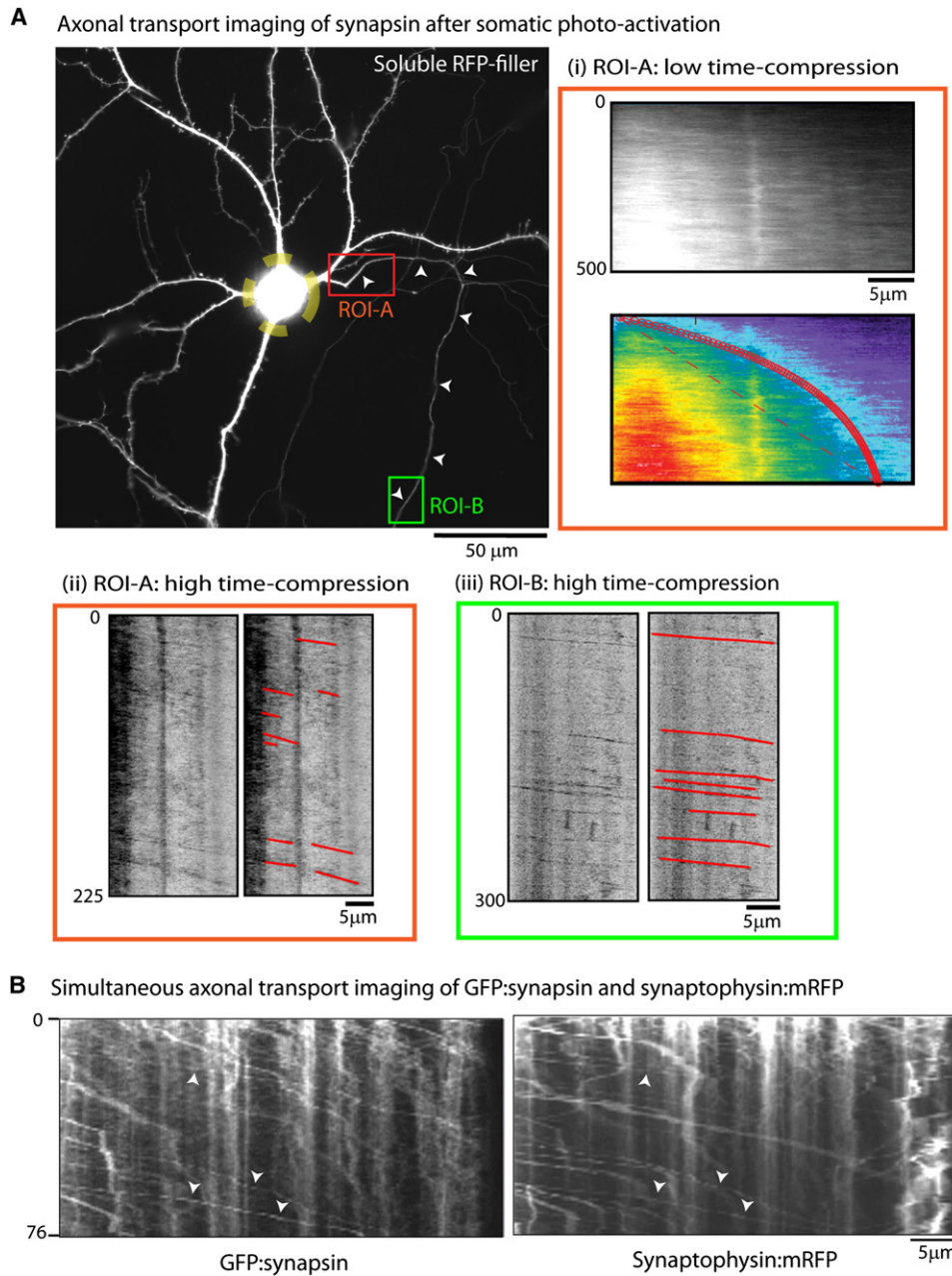


Figure 4. A Subset of Rapid and Persistent Synapsin Particles in Axons

(A) Neurons were cotransfected with PA-GFP:synapsin and soluble mRFP (to identify morphology, image on left) and the cell body was selectively photoactivated (dashed yellow circle marks the boundaries of the photoactivation zone; small arrowheads mark the emanating axon). Thereafter, the photoactivated protein pool was imaged as it entered the axon by using varying time compressions in proximal (ROI-A, red box) and distal (ROI-B, green box) regions. Imaging of the proximal axon in ROI-A at low time compressions (1 frame/5s) revealed a slow, anterogradely moving plume of fluorescence matching the known kinetics of slow transport (kymographs in panel i, slope = 0.02, equivalent to average velocity of 0.02 μ m/s). However, when the same ROI was imaged at a higher time compression (1 frame/0.75 s), we also saw rapid, persistent particles emerging from the front of the slowly migrating fluorescence plume (kymographs in panel ii). This was further confirmed by subsequent imaging of a distal portion of the same axon (ROI-B) at the higher frame rate, where many rapid and persistent particles were clearly seen moving with an exclusively anterograde bias (kymographs in panel iii). Axonal transport of the fast component protein APP by using a similar paradigm is shown in Figure S5.

(B) Simultaneous imaging of steady-state GFP:synapsin and synaptophysin:mRFP in thin distal axons revealed mostly persistent synapsin particles that colocalized with synaptophysin (arrowheads). Scale bars are in the lower right in each panel. Elapsed time in seconds is shown on the left of the kymograph.

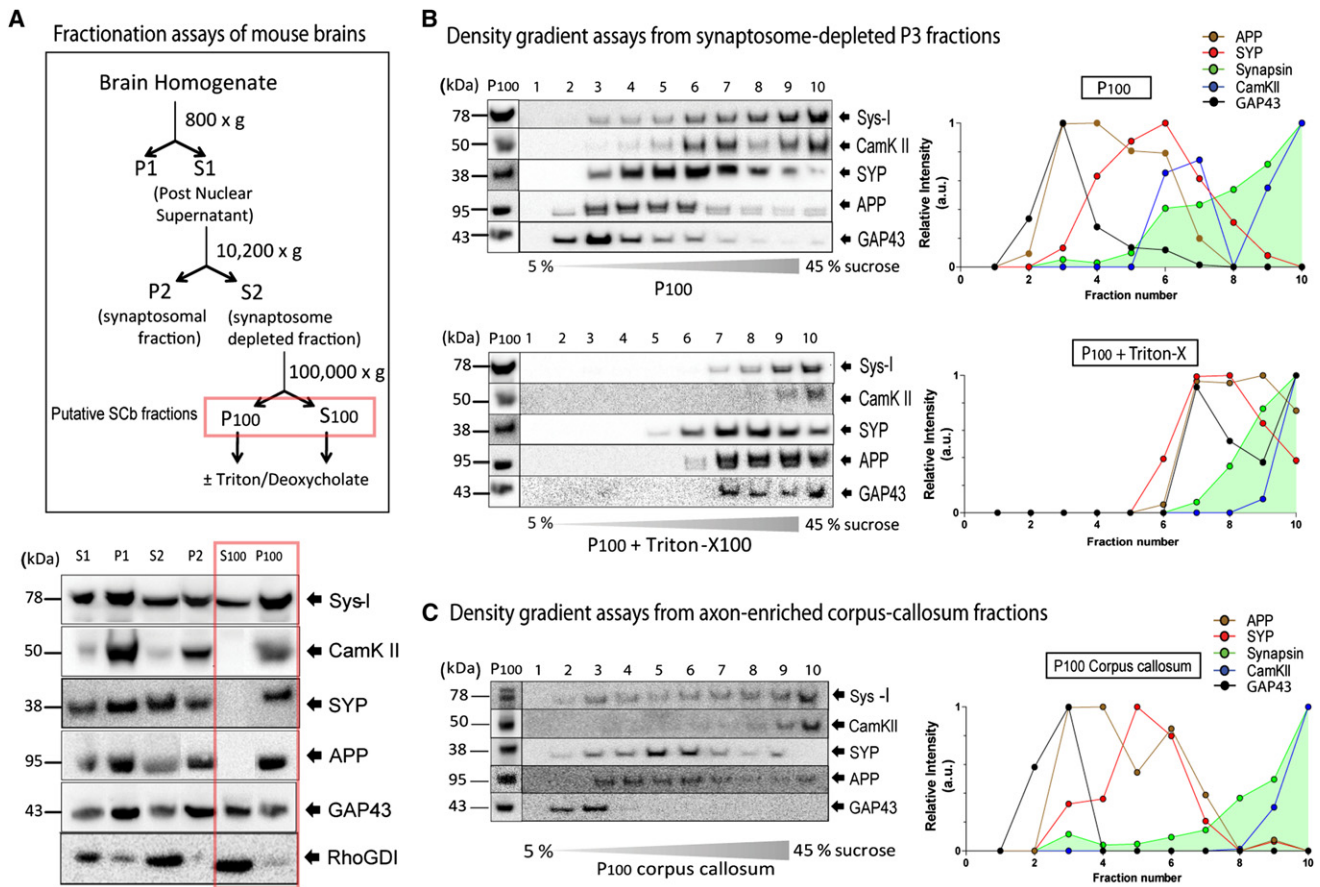


Figure 5. Biochemical Analysis of Synapsin and CamKII In Vivo from Axon-Enriched Fractions

(A) Mouse brains were homogenized and fractionated as outlined in the experimental strategy on the left, reasoning that axonal synapsin/CamKIIa cargoes would exist within P₁₀₀ and S₁₀₀ (derivates of S2, the synaptosome-depleted fractions, boxed in red). Fractions were blotted with antibodies to synapsin (Sys-I) and CamKII as well as the vesicular proteins synaptophysin (SYP), APP, and GAP-43. The gel below shows that large proportions of these proteins were also present in the high-speed pellet (P₁₀₀) indicating that they are not entirely soluble. Note that the presumably diffusive signaling molecule RhoGDI remains largely in the supernate in such experiments.

(B) Top: In density-gradient assays from the P₁₀₀ fractions, large populations of synapsin, and CamKII are found in the high-density fractions 7–10 (P₁₀₀) distinct from vesicular proteins. Bottom: Treatment of P₁₀₀ with Triton-X100 attenuated the associations of vesicular proteins with little effect on the higher density fractions containing synapsin/CamKII. Densitometry analysis of the gels is shown on the right.

(C) Similar supernate/pellet proportions and separation of cytosolic and vesicular proteins was observed in density gradients from axon-enriched corpus callosum fractions from mouse brains as well.

preparations from mouse brains (Figure 5C). In contrast, within the synaptosomal (P2) preparations, both synapsin and CamKII were largely (though not exclusively) associated with lighter fractions (Figure S6B) and this association was disrupted by detergent treatment (Figure S6C), suggesting that in synaptic domains these proteins are largely associated with synaptic vesicles (as expected). The presence of synapsin and CamK in higher density fractions within high-speed P₁₀₀ pellets and their resistance to detergents further suggest that synapsin and CamK in these fractions are organized into proteinaceous complexes.

Data-Driven Biophysical Simulation of Cytosolic Cargo Transport

Next we generated a biophysical simulation model of synapsin transport driven by our imaging data to test specific scenarios

that could not be readily addressed by experimentation. To simulate our photoactivation experiments we assumed an aqueous cylindrical environment (axon) containing hypothetical synapsin particles distributed within a central zone at time = 0 (Figure 6A, green particles), mimicking the photoactivated pool of synapsin molecules in our imaging experiments immediately after activation. At all times, each simulated synapsin particle was allowed to diffuse randomly within the axonal compartment with known diffusion coefficients of GFP:synapsin in axons (Tsuruel et al., 2006) and also to collide with other intracellular components. To further simulate our experimental data we allowed several hypothetical motor-driven “mobile units” to traverse along the axon (white spheres in Figures 6A and 6B; also see Movie S8). These mobile units were allowed to move persistently with a range of velocities similar to those seen in our “speckle-imaging” assays ($\leq 3 \mu\text{m/s}$, only a few anterograde

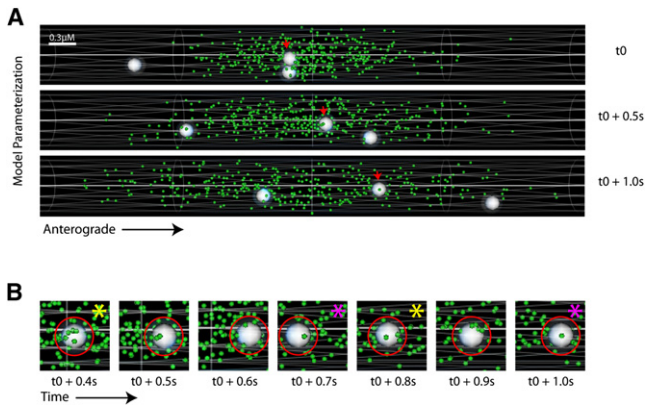


Figure 6. A Biophysical Simulation Model of Slow Axonal Transport

(A) A simulation model was developed as described in the text, consisting of a hypothetical axon cylinder, synapsin particles (green) distributed in the central zone, and vectorial mobile units (white spheres). The scale bar is shown in the upper left and elapsed time is to the right of the frames. Screen shots from a simulated time-lapse show mobile units traversing through a pool of synapsin particles; one anterogradely moving particle is marked with small red arrows (also see *Movie S7*).

(B) Dynamics of association/dissociation and clustering of synapsin particles on a mobile unit shown in representative zoomed screen shots from a simulated time-lapse. The red circle represents the dissociation radii around a mobile unit that restricts the movements of the synapsin particles that collide with the mobile units (see text). Note the stochastic clustering and dispersion of synapsin particles upon the mobile unit in successive frames, marked by yellow and magenta asterisks respectively.

units are shown in the figure for simplicity), shooting through the cluster of synapsin particles in the model. Besides free diffusion, the synapsin particles within the axon were allowed to either (1) randomly collide with vectorial mobile units as they passed through or (2) specifically associate with mobile units for user-defined probabilities of association to simulate the clustering and association behavior of particles that we found in our imaging experiments (*Figure S4*). Virtual kymographs and intensity-center shifts were generated from simulations (see *Experimental Procedures* for further details).

Three basic scenarios were simulated, as follows: (1) First we assumed that the synapsin molecules were only diffusing passively and randomly colliding with the bidirectional vectorial mobile units (*Figure 7A*, kymographs, top panel). No significant intensity-center shift was noted under these conditions (*Figure 7A*, graph, top panel). (2) Even when retrogradely moving particles were completely eliminated from the simulation, there was no significant shift in the intensity center (*Figure 7A*, bottom panel), indicating that nonspecific movement within the axonal shaft, even when polarized, is insufficient to create a population shift in this model. Recent studies have shown that movement of motor-driven cargoes can generate intracellular turbulence that can cause fluctuating motion of cytoskeletal polymers (*Brangwynne et al., 2007, 2008*) and it is possible that such motion can also generate transport of cytosolic proteins. However, these simulation data argue that the anterograde bias of synapsin seen in our experiments is unlikely to be generated simply by nonspecific movement of other fast and persistent particles

within the axonal shaft, but must involve additional mechanisms. Toward this, we next tested scenario (3), asking whether the intensity-center shifts in our imaging experiments could be simulated by assuming that the hypothetical synapsin particles were associating with (and subsequently clustering on) vectorial mobile units as they moved anterogradely.

Indeed, we found that introduction of this singular parameter to the simulation (ability to transiently associate) was sufficient to generate a vectorial shift in the synapsin population (*Figure 7B*). Furthermore, we found that the magnitude of the intensity-center shift correlated with changes in the interaction strengths between the synapsin particles and the mobile units (*Figure S7*), suggesting that such interactions were key determinants of intensity-center shifts. However, we found that when individual synapsin particles were allowed to associate with the mobile units with a constant interaction strength, the intensity-center shifts obtained rose linearly over time (*Figure 7B*, upper panels and *Figure S7*) and did not match the actual imaging data where the intensity shifts plateau after an initial rise (see graphs in *Figure 2*). Instead we found that to match the simulated intensity-center shifts to the experimental data, it was necessary to assign a range of interaction strengths to the synapsin particles as shown in *Figure 7B* (lower panels). *Figure 7C* shows further details of the simulation that most closely matched the actual imaging experiments.

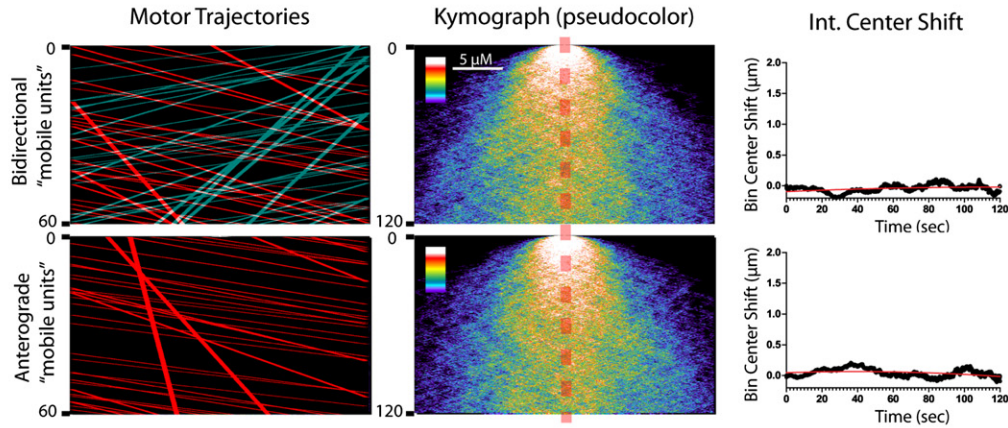
Collectively, the simulation results indicate that (1) the anterogradely biased motion of photoactivated synapsin molecules in our experiments is unlikely to be a result of a nonspecific axonal flow; (2) clustering of individual synapsin molecules into larger transport-competent supramolecular structures is necessary and sufficient to generate the biased vectorial motion of the synapsin population seen in our imaging experiments; and (3) the interaction strengths of synapsin molecules with the mobile units are not invariant, but likely encompass a range of interaction strengths.

DISCUSSION

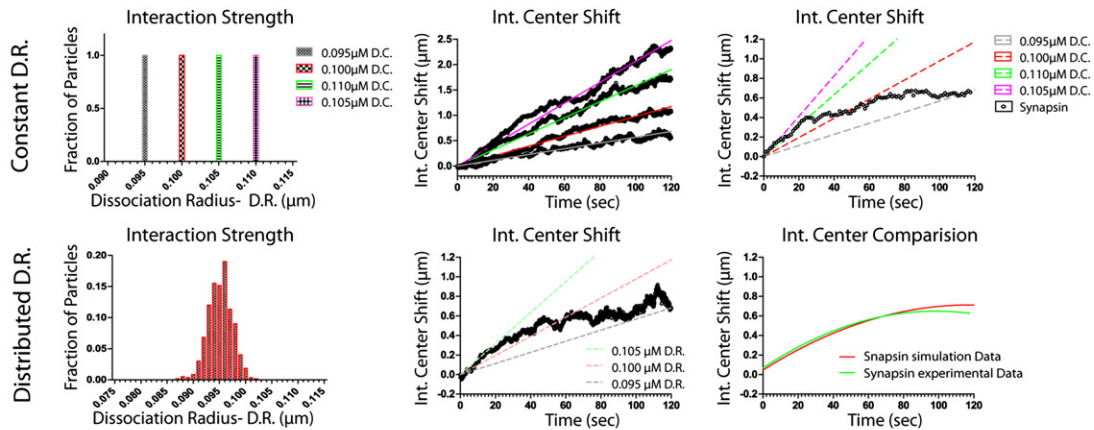
The Problem: How Are Cytosolic Proteins Delivered to Their Destinations?

Proteins are delivered into synapses by both fast and slow axonal transport (*Garner and Mahler, 1987*). However, while the basic principles underlying the fast axonal transport of vesicular proteins are well understood, mechanisms underlying the slow transport of cytosolic proteins that have much slower overall velocities are unclear. While previous pulse-chase radiolabeling studies have generally characterized the movement of these cytosolic cargoes, they have not provided much mechanistic insight into how such inherently soluble, cytosolic proteins can be conveyed slowly and efficiently along axons. Thus, though overall transport of synapsin and CamKIIa was described decades ago, to this date the underlying mechanisms that lead to this motion remain unclear. In this study we adopted an imaging strategy to visualize the bulk transport as well as single particle kinetics of the presynaptically enriched cytosolic cargoes synapsin and CamKIIa in living neurons, combining them with *in vivo* biochemical assays and data-driven computational modeling.

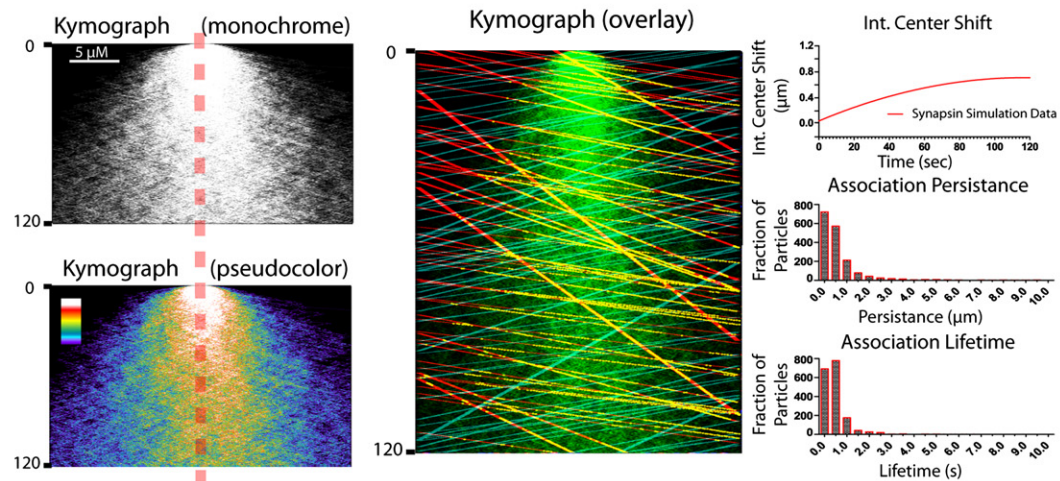
A Modeling “active diffusion” dynamics of synapsin particles



B Parameterizing specific associations of synapsin particles with mobile units



C Best-fit simulation of imaging data



Unconventional Transport Behavior of Cytosolic Proteins: Qualitative and Mechanistic Differences from Other Transport Modes

We found that pools of cytosolic cargoes are transported in a streaming fashion and with a motor-dependent anterograde bias very different from the stochastic transport of individual vesicles. This overall biased motion is likely generated by an intricate particle kinetics including transient assembly and short rapid vectorial spurts (Figure S4), very different from fast vesicular transport, which is typically persistent. The anterograde bias of the population, the dependence on molecular motors, the dissimilarity of cytosolic cargo motion to untagged PAGFP, the short-range, rapid vectorial speckle movement, and the modeling data all argue that this movement is not entirely a simple diffusive process. In brains, we found that these proteins are also present within high-speed pellet fractions, migrate distinctly from vesicular proteins in density gradients, and are resistant to detergent treatments that solubilize membranes. Finally, our modeling data suggest that clustering of these cytosolic proteins is necessary and sufficient to generate the vectorial shift seen in our imaging experiments.

Collectively, the imaging, biochemical, and biophysical data support the following scenario. After synthesis, a small fraction of soluble proteins associate with vesicles and are rapidly transported (at least for vesicle-associated proteins like synapsins). However, the bulk of soluble proteins transiently assemble into supramolecular assemblies like multiprotein complexes that are conveyed by associations with molecular motors. This association may be direct or indirectly mediated via association with vesicles (note partial overlap of cytosolic cargoes with vesicles in Figures 5B and 5C). We are struck by the peculiarity of this slower motion when compared to other modes of intracellular transport, axonal transport or otherwise. In the classic mode of vesicular transport, for instance, individual vesicles bind to motors and the motor-cargo unit is then transported stochastically for long distances. In the case of cytosolic proteins, however, fluorescent molecules are transported in streaming plumes, qualitatively distinct from other transport modalities. As cytosolic proteins are ubiquitous, it is tempting to speculate that all cell types employ such mechanisms to convey them to their destinations within the cell.

The Role of Diffusion in the Axonal Transport of Cytosolic Cargoes

Unlike membranous proteins that are anchored to vesicles, cytosolic proteins invariably have diffusible pools, raising the question of whether diffusion can play a role in cytosolic cargo transport (Miller and Heidemann, 2008). In that regard, recent studies have revealed an intracellular motion where random intracellular agitation from the activity of motors can create cytoplasmic stirring that can then move proteins in its wake (Brangwynne et al., 2008, 2009). In the context of cytosolic cargo transport, it seems plausible that soluble, freely diffusible molecules of cytosolic proteins can be simply transported secondary to a polarized flow generated by other moving organelles, as opposed to specific interactions of higher order structures (like cargo complexes) with motors.

Several observations argue against this notion. First, though individual cargoes can exhibit a biased transport in axons, when overall axonal transport is examined (as in the squid and *Xenopus* system), a plethora of organelles are seen to move bidirectionally and there is little evidence of a bias in overall movement (Grafstein and Forman, 1980). Thus there is no reason to believe that there is a biased flow within axons in the steady-state situation. Even if we assume that there was some polarized axonal flow that could carry soluble proteins in its wake, one would expect that a purely soluble protein with no significant molecular interactions within neurons would be conveyed by such mechanisms. However, as shown in Figure 1C, soluble untagged PAGFP has no bias in axons. Second, average velocities of mobile speckles within the photoactivated pool ($\approx 1 \mu\text{m/s}$) encompass the expected range of motor-driven cargoes (Figure S4), which would be difficult to reconcile if the motion was solely generated by passive flows. Furthermore, the wide diversity of axonal transport rates seen in our studies indicates an overall motion that would also be inconsistent with a polarized flow, which would probably generate homogeneous transport velocities. Finally, in our biophysical modeling, we specifically simulated situations that would be analogous to passive flows within the axon, allowing hypothetical mobile units to move within the simulation and physically collide with the cytosolic particles, but as shown in Figure 7A, such passive movements were not sufficient to generate any biased flow of

Figure 7. Data-Driven Modeling of Specific Transport Scenarios

Various parameters were introduced into the simulation model to test specific scenarios that could not be readily addressed by experimentation and the data output was analyzed by using kymographs and intensity-center analysis as described in the text. In all cases, synapsin particles were allowed to undergo Brownian motion and biophysical collisions.

(A) Kymographs on the left show anterograde (red tracks) and/or retrograde (blue tracks) mobile units traversing across a simulated axon containing synapsin particles. Kymographs in the middle show the dispersion of synapsin particles and the graphs on the right show the corresponding intensity-center shifts. Note that these simulation parameters are not sufficient to generate a shift in the intensity center.

(B) In these simulations, specific interactions were allowed between the synapsin particles and the mobile units by creating a dissociation radii around the mobile units as detailed in the Experimental Procedures. Alteration of dissociation radii led to changes in hypothetical interaction strengths allowing us to test the effects of a range of interaction strengths in the simulation. Assumption of such interactions was necessary and sufficient to generate an anterograde shift of the synapsin population. However, when we assumed invariable dissociation radius/interaction strengths in the simulation, the intensity-center shifts were continuously linear and did not match the actual imaging data as shown in the top panels (also see Figure S7). Instead, the imaging data was best fitted by assuming a range of interactions as shown in the bottom panels.

(C) Detailed data from the simulation above that best fitted the actual imaging data. Note the anterograde shift of the synapsin population qualitatively seen in the kymographs (left). In the simulated multiple-parameter overlaid kymograph (middle), synapsin particles are shown in green and tracks of anterograde and retrograde mobile units are depicted in red and blue, respectively. The yellow tracks represent instances of colocalization of anterograde mobile unit tracks (red) and synapsin particles (green). Note the numerous instances of transient associations and vectorial motion evident in this kymograph. Graphs on the right show the various other outcomes of the simulation.

the population. Instead, shifts in the simulated population were only possible when we assumed specific interactions between the cytosolic molecules and the mobile units. In fact, we could alter the magnitudes of the shifts in the population simply by altering the association and dissociation rates between the synapsin particles and the mobile units in the model (Figure S7), suggesting that such interactions were necessary and sufficient to create the biased population dynamics in our studies.

Thus, though there is good evidence that diffusion can generate some intracellular motion such as fluctuation of cytoskeletal polymers (Brangwynne et al., 2007) and it is clear that cytosolic proteins can diffuse, we favor the view that though passive diffusion is a component of cytosolic cargo transport simply because of the biophysical properties of these proteins, such mechanisms do not actively contribute to the vectorial slow transport seen within axons.

A Working Model for Intracellular Transport of Soluble Cargos

Based on the data, we propose a model for the axonal transport of cytosolic synaptic cargoes where soluble proteins dynamically organize into multiprotein complexes that are conveyed by motors. Our biophysical simulations provide substantial support for the overall model by showing that clustering and/or associations of freely diffusible synapsin molecules are necessary and sufficient to generate the anterograde flux seen in our imaging experiments. The existence of protein complexes is supported by the following data: (1) Imaging experiments directly reveal assembly and vectorial transport of punctate fluorescent speckles containing these proteins (Figure S4). (2) Such particles are also seen natively by immunostaining (Figure S1). (3) Upon motor inhibition, we saw clusters of stalled synapsin and CamKIIa particles clearly in axons (Figure 3B), suggesting that their mobility was interrupted by these manipulations. (4) Finally, biochemical experiments show that subsets of these cytosolic proteins are present in high-speed pellets from synaptosome-depleted (P_{100}) as well as axon-enriched corpus callosum brain fractions that are detergent resistant, indicating the existence of higher order macromolecular structures within axons *in vivo* (Figure 5). We posit that the vast majority of these complexes transiently engage with motors (directly or indirectly) within axons, leading to a slow overall movement of the synapsin/CamKIIa population.

Minor Fractions of Synapsin Are Cotransported with Vesicles in Fast Axonal Transport

Early nerve ligation/crushing studies showed that synapsin was associated with vesicles accumulating proximally in ligated/crushed sites (Böök et al., 1986). More detailed pulse-chase radiolabeling studies showed that while a small population of newly synthesized synapsin ($\approx 15\%$) departed the soma immediately afterwards, the vast majority ($\approx 85\%$) was released from the cell body only after several days, and this pool moved much more slowly, at rates consistent with slow axonal transport (Baitinger and Willard, 1987; Petrucci et al., 1991). More recent studies have shown that in cultured neurons, synapsin is associated with mobile synaptic vesicular precursors (transport packets) probably conveyed in fast axonal transport (Ahmari

et al., 2000). Synapsin is also an established component of synaptic vesicles (Takamori et al., 2006).

Our data (Figure 4A) directly show that photoactivated somatic synapsin is transported into proximal axons both as punctate particles that are highly persistent and as a slow wave that departs the soma with a transport behavior consistent with slow axonal transport. The persistent punctate synapsin particles colocalize with synaptophysin, a vesicular protein conveyed in fast axonal transport (Figure 4B). Collectively, the data indicate that a small fraction of newly synthesized synapsin is associated with vesicles and conveyed in fast axonal transport, while the remainder is conveyed in slow axonal transport with intricate particle kinetics. Though the biological basis for this bimodal transport behavior is unclear, it may have some evolutionary significance, in which cytosolic proteins in higher organisms may have acquired novel roles at synapses that require them to quickly localize to boutons, necessitating rapid transport in the fast component as well.

In contrast to vesicular transport, mechanisms of slow axonal transport have been harder to unravel, largely because of difficulties in visualizing the phenomena (Brown, 2003). This is particularly true for transport of cytosolic cargoes where the inherent solubility of these proteins makes optical imaging challenging. In previous studies, we transfected fluorescent-tagged soluble proteins in cultured hippocampal neurons and imaged thin distal axons, visualizing discernible individual particles within a diffuse background of fluorescent molecules (Roy et al., 2007, 2008). Based on observations that cytosolic particles moved rapidly but more infrequently than fast component proteins, we speculated that population dynamics of cytosolic cargoes were akin to neurofilament transport, in which compelling evidence indicates that the intermittent fast movements of individual neurofilaments leads to the overall slow rates seen in the radiolabeling studies (Roy et al., 2000; Wang et al., 2000; Yan and Brown, 2005). However, limited to the analysis of observable particles in thin distal axons, our previous methods did not allow us to visualize and analyze the population as a whole or consider potential roles of nonparticulate or diffusible protein pools on overall transport, an issue that we overcame by using our current imaging paradigm. Moreover, these studies did not take into account the minor pools of cytosolic proteins moving in fast transport. In hindsight, it seems probable that the vast majority of the transient, short-range movements that we see with our photoactivation paradigm were not apparent with steady-state labeling, where they were perhaps hidden within the background fluorescence. The presence of fast-moving particles also complicates the interpretation of our previous studies. Finally, some studies have reported the biased movement of soluble, cytoskeletal proteins in extruded squid axons by exogenously introducing (stabbing) these proteins within the axon shaft (Galbraith et al., 1999; Terada et al., 2000). The physiologic relevance of this experimental paradigm is unclear and these studies do not provide much mechanistic insight beyond what is known from using pulse-chase radiolabeling.

In summary, our experiments with live imaging, *in vivo* biochemical assays, and biophysical modeling suggest a working model that can explain the mechanistic logic behind the slow axonal transport of cytosolic proteins. Though the model can

explain how clusters of cytosolic proteins can be transported efficiently, further insights into the rules of cytosolic protein transport will have to await identification of specific transport machineries and the detailed characterization of the complexes themselves.

EXPERIMENTAL PROCEDURES

Hippocampal Cell Cultures, Transfections, and Plasmids

Hippocampal cultures were obtained from brains of postnatal (P0–P2) CD-1 mice following standard protocols. Briefly, dissociated cells were plated at a density of 50,000 cells/cm² in poly-D-lysine-coated glass-bottom culture dishes (MatTek, Ashland, MA) and maintained in Neurobasal + B27 media (Invitrogen, Carlsbad, CA) supplemented with 0.5 mM glutamine. Neurons were transiently transfected with the respective PAGFP construct and a soluble mRFP (to identify transfected neurons) by using Lipofectamine 2000 (Invitrogen) at 7–9 days in vitro (DIV) according to the manufacturer's instructions. All axonal transport studies were performed 17–24 hr after transfection. For CamKIIa, some neurons were allowed to express the proteins for up to 48 hr because of low levels of PA protein pools (empiric observations). All animal studies were performed in accordance with University of California guidelines. The GFP:synapsin-Ia and the APP constructs were subcloned into the PAGFP vector by using standard cloning techniques. All constructs used in this study were confirmed by sequencing.

Microscopy, Live Imaging, and Photoactivation Setup

All time-lapse images were acquired by using an Olympus IX81 inverted motorized epifluorescence microscope equipped with a Z-controller (IX81, Olympus), a motorized X-Y stage controller (Prior Scientific), and a fast electronic shutter (Smartshutter). Images were acquired by using an ultrastable light source (EXFO X-Cite) and CCD cameras (Coolsnap HQ², Photometrics); photoactivation was performed by using a 100 W mercury lamp (Olympus). For live imaging, neurons were transferred to a live-cell imaging media containing low-fluorescence Hibernate E (Brainbits), 2% B27, 2 mM Glutamax, 0.4% D-glucose, and 37.5 mM NaCl (Roy et al., 2008) and maintained at 37°C by using an air-curtain incubator (Nevtek) mounted on the microscope. All images were acquired by using Metamorph software (Molecular Devices) and processed by using either Metamorph or Matlab (MathWorks). For simultaneous photoactivation and visualization, we used the IX2-RFAW, dual-input illuminator (Olympus) attached to the microscope. The photoactivation input contained a violet excitation filter (D405/40, Chroma), a pinhole to focus the incident activation beam, and an electronic shutter (Olympus) in the light path. The visualization input contained a GFP excitation filter (HQ480/40, Chroma) and a neutral-density filter (reducing the incident-light intensity by 94%–97%). The GFP filter cube within the microscope housing consisted of (1) a dichroic mirror (T495pxr, Chroma) that blocked transmission of (and reflected) low-wavelength violet light and (2) an emission filter (HQ535/50, Chroma). By using these settings we were able to photoactivate our region of interest while visualizing it. Consistent imaging parameters were used throughout all experiments.

Quantitative Image Analyses: Intensity-Center Analysis

The intensity-center analysis function represents the arithmetic peak of the mean values of fluorescence intensities along the photoactivated zone and was determined as follows. After background subtraction, the photoactivated ROI was cropped. An average-intensity line scan was then performed within this ROI to generate kymographs by using Metamorph. Subsequent analysis was performed in MatLab. Line scans representing each time point within the kymograph were subjected to the following equation to assay the intensity center of the pulse-labeled protein population at each time point: $([X_1, X_2, X_3, \dots, X_n] \times [I_1, I_2, I_3, \dots, I_n]) / \text{sum}([I_1, I_2, I_3, \dots, I_n])$. Here, $[X_1, X_2, X_3, \dots, X_n]$ defines an array of X coordinates of pixels along the axon from 1 to X_n, where X_n represents the length of the photoactivated zone. $[I_1, I_2, I_3, \dots, I_n]$ defines an array representing the intensity at each X coordinate. These intensity-center values were then normalized by subtracting the X coordinate of the intensity center at t = 0 from the intensity center at each subsequent time point. The data were then graphically represented as intensity-center shift versus time.

Biochemical Assays

For fractionation assays, brains from 4-week-old CD-1 mice were homogenized in buffer containing 20 mM HEPES, 40 mM KCl, 5 mM EGTA, 5 mM EDTA, and protease inhibitors (pH 7.2). The resulting homogenate was centrifuged at 1000 g for 20 min to obtain a nuclear pellet (P1) and a postnuclear supernatant (S1). The supernatant S1 was centrifuged at 10,200 g for 20 min to obtain the crude synaptosomal fraction (P2) and synaptosome-depleted fraction (S2). Finally, the S2 supernatant was then centrifuged at high speeds (100,000 g for 1 hr at 4°C) to obtain supernatant S100 and pellet P100. For floatation assays, P100 fractions were adjusted to 45% sucrose, bottom-loaded on a 5%–45% sucrose gradient, and centrifuged at 160,000 g for 16 hr at 4°C in a SW55-Ti swinging bucket rotor in an Optima L-100 ultracentrifuge (Beckman-Coulter). Ten fractions (0.5 ml each) were collected from the top of the gradient column and equal volumes were used for SDS-PAGE and western blot analysis. For some experiments, 1% Triton X-100 or 1% deoxycholate was added and floatation assays were performed as mentioned above. The following antibodies were used for western blotting: anti-Synapsin-I at 1:5000 (Synaptic Systems), anti-APP at 1:2000 (Epitomics), anti-CamKII at 1:2000 (Thermo Scientific), anti-synaptophysin at 1:1000 (Millipore, USA), and anti-GAP43 (sc-17790, Santa Cruz). Blots were developed by using Pierce Fast Western Blot Kit ECL Substrate, visualized by using Versa Doc Imaging system (Bio-Rad), and quantified by densitometry.

Computational Modeling of Slow Axonal Transport

Details regarding generating the simulation and analyzing the data are provided in the Supplemental Experimental Procedures.

Statistical Methods

Routine statistics were used to analyze data and are indicated in the respective figure legends.

SUPPLEMENTAL INFORMATION

Supplemental Information includes Supplemental Experimental Procedures, seven figures, and eight movies and can be found with this article online at [doi:10.1016/j.neuron.2011.03.022](https://doi.org/10.1016/j.neuron.2011.03.022).

ACKNOWLEDGMENTS

This work was supported by start-up funds from University of California, San Diego and grants from the March of Dimes foundation (Basil O'Connor) and NIH (P50AG005131-project 2) to S.R. The authors thank Dr. Ge Yang (Carnegie Mellon University) for his suggestion of and initial assistance with the intensity-center analysis. We are grateful to Drs. Patterson and Lippincott Schwartz (National Institutes of Health) for the PAGFP construct. We also thank Drs. George Augustine (Duke University), Bernardo Sabatini (Harvard), Christoph Kaether (Leibniz Institute, Germany) and Leon Lagnado (Medical Research Council, Cambridge, UK) for providing the GFP:synapsin-I, PAGFP:CamKIIa, APP:YFP, and synaptophysin:mRFP respectively.

Accepted: March 11, 2011

Published: May 11, 2011

REFERENCES

- Ahmari, S.E., Buchanan, J., and Smith, S.J. (2000). Assembly of presynaptic active zones from cytoplasmic transport packets. *Nat. Neurosci.* 3, 445–451.
- Baitinger, C., and Willard, M. (1987). Axonal transport of synapsin I-like proteins in rabbit retinal ganglion cells. *J. Neurosci.* 7, 3723–3735.
- Böök, S., Larsson, P.A., Dahllöf, A.G., and Dahlström, A. (1986). Axonal transport of synapsin I- and cholinergic synaptic vesicle-like material; further immunohistochemical evidence for transport of axonal cholinergic transmitter vesicles in motor neurons. *Acta Physiol. Scand.* 128, 155–165.
- Brangwynne, C.P., MacKintosh, F.C., and Weitz, D.A. (2007). Force fluctuations and polymerization dynamics of intracellular microtubules. *Proc. Natl. Acad. Sci. USA* 104, 16128–16133.

- Brangwynne, C.P., Koenderink, G.H., MacKintosh, F.C., and Weitz, D.A. (2008). Cytoplasmic diffusion: Molecular motors mix it up. *J. Cell Biol.* *183*, 583–587.
- Brangwynne, C.P., Koenderink, G.H., MacKintosh, F.C., and Weitz, D.A. (2009). Intracellular transport by active diffusion. *Trends Cell Biol.* *19*, 423–427.
- Brown, A. (2003). Axonal transport of membranous and nonmembranous cargoes: A unified perspective. *J. Cell Biol.* *160*, 817–821.
- Dorn, J.F., Danuser, G., and Yang, G. (2008). Computational processing and analysis of dynamic fluorescence image data. *Methods Cell Biol.* *85*, 497–538.
- Dunkley, P.R., Jarvie, P.E., and Robinson, P.J. (2008). A rapid Percoll gradient procedure for preparation of synaptosomes. *Nat. Protoc.* *3*, 1718–1728.
- Fletcher, T.L., Cameron, P., De Camilli, P., and Banker, G. (1991). The distribution of synapsin I and synaptophysin in hippocampal neurons developing in culture. *J. Neurosci.* *11*, 1617–1626.
- Galbraith, J.A., Reese, T.S., Schlieff, M.L., and Gallant, P.E. (1999). Slow transport of unpolymerized tubulin and polymerized neurofilament in the squid giant axon. *Proc. Natl. Acad. Sci. USA* *96*, 11589–11594.
- Garner, J.A., and Lasek, R.J. (1982). Cohesive axonal transport of the slow component b complex of polypeptides. *J. Neurosci.* *2*, 1824–1835.
- Garner, J.A., and Mahler, H.R. (1987). Biogenesis of presynaptic terminal proteins. *J. Neurochem.* *49*, 905–915.
- Gitler, D., Xu, Y., Kao, H.T., Lin, D., Lim, S., Feng, J., Greengard, P., and Augustine, G.J. (2004). Molecular determinants of synapsin targeting to presynaptic terminals. *J. Neurosci.* *24*, 3711–3720.
- Grafstein, B., and Forman, D.S. (1980). Intracellular transport in neurons. *Physiol. Rev.* *60*, 1167–1283.
- Kaether, C., Skehel, P., and Dotti, C.G. (2000). Axonal membrane proteins are transported in distinct carriers: A two-color video microscopy study in cultured hippocampal neurons. *Mol. Biol. Cell* *11*, 1213–1224.
- Kimura, T., Watanabe, H., Iwamatsu, A., and Kaibuchi, K. (2005). Tubulin and CRMP-2 complex is transported via Kinesin-1. *J. Neurochem.* *93*, 1371–1382.
- Kleim, J.A., Bruneau, R., Calder, K., Pocock, D., VandenBerg, P.M., MacDonald, E., Monfils, M.H., Sutherland, R.J., and Nader, K. (2003). Functional organization of adult motor cortex is dependent upon continued protein synthesis. *Neuron* *40*, 167–176.
- Kozielski, F., Sack, S., Marx, A., Thormählen, M., Schönbrunn, E., Biou, V., Thompson, A., Mandelkow, E.M., and Mandelkow, E. (1997). The crystal structure of dimeric kinesin and implications for microtubule-dependent motility. *Cell* *91*, 985–994.
- Lasek, R.J., Garner, J.A., and Brady, S.T. (1984). Axonal transport of the cytoplasmic matrix. *J. Cell Biol.* *99*, 212s–221s.
- Lillemeier, B.F., Köster, M., and Kerr, I.M. (2001). STAT1 from the cell membrane to the DNA. *EMBO J.* *20*, 2508–2517.
- Lund, L.M., and McQuarrie, I.G. (2001). Calcium/calmodulin-dependent protein kinase IIalpha in optic axons moves with slow axonal transport and undergoes posttranslational modification. *Biochem. Biophys. Res. Commun.* *289*, 1157–1161.
- Lund, L.M., and McQuarrie, I.G. (2002). Calcium/calmodulin-dependent protein kinase IIbeta isoform is expressed in motor neurons during axon outgrowth and is part of slow axonal transport. *J. Neurosci. Res.* *67*, 720–728.
- Miller, K.E., and Heidemann, S.R. (2008). What is slow axonal transport? *Exp. Cell Res.* *314*, 1981–1990.
- Paggi, P., and Petrucci, T.C. (1992). Neuronal compartments and axonal transport of synapsin I. *Mol. Neurobiol.* *6*, 239–251.
- Petrucci, T.C., Macioce, P., and Paggi, P. (1991). Axonal transport kinetics and posttranslational modification of synapsin I in mouse retinal ganglion cells. *J. Neurosci.* *11*, 2938–2946.
- Pfister, K.K., Wagner, M.C., Bloom, G.S., and Brady, S.T. (1989). Modification of the microtubule-binding and ATPase activities of kinesin by N-ethylmaleimide (NEM) suggests a role for sulfhydryls in fast axonal transport. *Biochemistry* *28*, 9006–9012.
- Roy, S., Coffee, P., Smith, G., Liem, R.K., Brady, S.T., and Black, M.M. (2000). Neurofilaments are transported rapidly but intermittently in axons: Implications for slow axonal transport. *J. Neurosci.* *20*, 6849–6861.
- Roy, S., Zhang, B., Lee, V.M., and Trojanowski, J.Q. (2005). Axonal transport defects: A common theme in neurodegenerative diseases. *Acta Neuropathol.* *109*, 5–13.
- Roy, S., Winton, M.J., Black, M.M., Trojanowski, J.Q., and Lee, V.M. (2007). Rapid and intermittent cotransport of slow component-b proteins. *J. Neurosci.* *27*, 3131–3138.
- Roy, S., Winton, M.J., Black, M.M., Trojanowski, J.Q., and Lee, V.M. (2008). Cytoskeletal requirements in axonal transport of slow component-b. *J. Neurosci.* *28*, 5248–5256.
- Shakiryanova, D., Tully, A., Hewes, R.S., Deitcher, D.L., and Levitan, E.S. (2005). Activity-dependent liberation of synaptic neuropeptide vesicles. *Nat. Neurosci.* *8*, 173–178.
- Sturgill, J.F., Steiner, P., Czervionke, B.L., and Sabatini, B.L. (2009). Distinct domains within PSD-95 mediate synaptic incorporation, stabilization, and activity-dependent trafficking. *J. Neurosci.* *29*, 12845–12854.
- Takamori, S., Holt, M., Stenius, K., Lemke, E.A., Grønborg, M., Riedel, D., Urlaub, H., Schenck, S., Brügger, B., Ringler, P., et al. (2006). Molecular anatomy of a trafficking organelle. *Cell* *127*, 831–846.
- Terada, S., Kinjo, M., and Hirokawa, N. (2000). Oligomeric tubulin in large transporting complex is transported via kinesin in squid giant axons. *Cell* *103*, 141–155.
- Tsuriel, S., Geva, R., Zamorano, P., Dresbach, T., Boeckers, T., Gundelfinger, E.D., Garner, C.C., and Ziv, N.E. (2006). Local sharing as a predominant determinant of synaptic matrix molecular dynamics. *PLoS Biol.* *4*, e271.
- Uchida, A., Alami, N.H., and Brown, A. (2009). Tight functional coupling of kinesin-1A and dynein motors in the bidirectional transport of neurofilaments. *Mol. Biol. Cell* *20*, 4997–5006.
- Wang, L., Ho, C.L., Sun, D., Liem, R.K., and Brown, A. (2000). Rapid movement of axonal neurofilaments interrupted by prolonged pauses. *Nat. Cell Biol.* *2*, 137–141.
- Whittaker, V.P. (1993). Thirty years of synaptosome research. *J. Neurocytol.* *22*, 735–742.
- Withers, G.S., George, J.M., Banker, G.A., and Clayton, D.F. (1997). Delayed localization of synelfin (synuclein, NACP) to presynaptic terminals in cultured rat hippocampal neurons. *Brain Res. Dev. Brain Res.* *99*, 87–94.
- Yan, Y., and Brown, A. (2005). Neurofilament polymer transport in axons. *J. Neurosci.* *25*, 7014–7021.
- Zeng, X., Goetz, J.A., Suber, L.M., Scott, W.J., Jr., Schreiner, C.M., and Robbins, D.J. (2001). A freely diffusible form of Sonic hedgehog mediates long-range signalling. *Nature* *411*, 716–720.

Neuron, Volume 70

Supplemental Information

Mechanistic Logic Underlying the Axonal

Transport of Cytosolic Proteins

David A. Scott, Utpal Das, Yong Tang, and Subhojit Roy

SUPPLEMENTAL EXPERIMENTAL PROCEDURES

Computational Modeling of Synapsin Transport: Generating the Simulation

The overall objective of our modeling was to test specific hypotheses that were not readily addressed by experimentation. The basic platform was an adaptation of a simulated 3-D biophysical environment developed by Jonathan B. Alberts, University of Washington (ParMspindle, source-code available at: <http://celldynamics.org/celldynamics/downloads/simcode.html>). This basic environment simulated intra-cellular movements of heterogeneous particle populations subject to Brownian and collision forces in an aqueous solution. The biophysical environment was implemented using pairwise Lagrange multipliers to calculate translational forces on particles induced by either collision events or Brownian forces. Brownian forces for particles in the system were defined as the diffusion coefficient for synapsin (Tsuruel et al., 2006), and collision forces were defined as the an instance of one particle impinging on another, and forces induced by collision events were calculated to reflect the magnitude of impingement of one particle on another. The model consisted of three main components- the axon, the synapsin particles and the “mobile-units”. 1) Axon: The simulated axon was defined as a 1mm long segment of axon with a radius of 0.25 μm derived from measurements of axon radii from 100X images of cultured hippocampal neurons. The aeta parameter defining the viscosity of the axoplasm was defined as $1e^{-3}$ to simulate an aqueous environment. 2) Synapsin particles: The diffusion coefficient of GFP:synapsin molecules in cultured hippocampal axons is known (Tsuruel et al., 2006). To determine the size of synapsin particles in the model that would resemble the in-situ biophysical properties of synapsin molecules in real axons, we simulated the mobility of pools of synapsin particles of incremental sizes, starting from a minimum radius of 0.14 μm , until we obtained a radius for the moving synapsin population that closely approximated the diffusion coefficient of 1.2 $\mu\text{m}^2/\text{s}$ in axons as determined by Tsuruel et al.. Thus a particle radius of ~0.023 μm was pseudo-empirically determined and used in all simulations. 3) Mobile-Units: Anterograde “mobile-units” (0.07 μm in diameter) were added to the system and parameterized to move along linear vectors running proximal to distal along the length of the simulated axon. Starting coordinates for the anterograde motor units were distributed pseudo-randomly in a uniform distribution throughout the proximal half of the axon at an initial density of ~3 mobile-units/10 μm axon with velocities generated from a pseudo-random uniform distribution varying between 0 and 3.0 $\mu\text{m}/\text{s}$ to simulate the stochastic nature of vectorial movements derived from fluorescent speckle tracking of vectorial synapsin movements in living axons. Retrograde mobile-units were added similarly.

Calculations for the vectorial movement of mobile-units in the system, the diffusion of SCb particles, and biophysical particle collisions were carried out at a time compression of 1ms in the model, and the system state was captured at a time compression of 100ms for use in analytical data structure production. 1ms was chosen to facilitate the sensitive approximation of all particle dynamics simulated in the system, while maintaining a tractable computational overhead for individual instances of the simulation at runtime. A 100ms time compression was chosen to approximate minimum feasible time compression for the gathering of time-lapse images from live imaging studies of the kinetics of photo-activated pulses of fluorescently labeled synapsin particles in our imaging experiments. Following the above parameterization, specific scenarios were tested to test passive diffusion alone and in the presence of antero- and/or retrograde vectorial mobile-units as described in the results. Next we tested the additive effects of specific interactions between anterograde mobile-units and synapsin particles to the biophysical components of the system. To parameterize such interactions, we restricted the dispersion of the synapsin particles after collision by assigning a constant “dissociation radius” to each mobile unit.

The dissociation radius is a hypothetical (parameterized, see below) “halo” around a mobile unit that restricts the dissociation of synapsin particles within the halo due to random biophysical/Brownian motion of synapsin particles that collide with a given mobile unit. Thus, assuming a collision event at $t=0$ ms, the ability of a given synapsin particle to remain associated with a mobile unit following a collision event is determined by the ability of the biophysical/Brownian forces of the particle to overcome the restrictions imposed by the dissociation radii at $t=0.1$ ms. Accordingly, if the displacement of the synapsin particle and its associated mobile unit was less than or equal to the defined distance of dissociation, the particle remained bound to the mobile unit. Thereafter, the synapsin particle proceeded in the vectorial path along with the mobile unit until the random biophysical forces acting on the particle at successive time-points resulted in a displacement that was greater than the dissociation radii; separating it from the mobile unit.

Computational Modeling of Synapsin Transport: Analyzing the Simulation Data

Intensity-center analysis and kymographs were then generated from the simulated data sets as follows. Kymograph images were constructed retrospectively from 100ms time compression state captures taken over the course of the simulation, which contain the 3-space coordinates of the initial and instantaneous coordinates of each of each mobile unit or SCb particle in addition to the object type, radius and logical association status (1,0) for each frame. This array of state capture data was subjected to particle tracking, which employed 4-space coordinates (containing x,y,z spatial coordinates and association state) to link individual object trajectories, object radii, and association states over the course of the simulation. Tracking data was saved to ANSI encoded data structures separated by object type, which were then translated into separate kymographs for each population of objects in the system as follows using Matlab: first, the 4-space data was subjected to y and z projections to generate 2 dimensional coordinate sets containing the x dimension of each particle and its association state for each time-point assayed in the simulation. Therefore, a $30\mu\text{m}$ (469px at simulated 100X conversion factor of $0.064\mu\text{m}/\text{px}$; the selected conversion factor was selected for consistency with constraints on in vitro data, while the resolution of the model system far exceeds that of the 100X objective used in our imaging studies) by 120s (1201px at 100ms time-compression) kymograph image was created as a 16bit matrix of zero values to provide a consistent frame of reference as used in analysis of intensity-center shifts of fluorescently labeled synapsin proteins from live imaging studies. Thus, the tracks for each particle were traversed, and the array of pixels of the particle diameter centered at the particle x-coordinate for each frame was incremented by 10 AFU. This process was repeated for all objects of a specific type tracked in the system. The resulting kymograph images constituted analytical equivalents to kymographs generated from live imaging data of fluorescently labeled synapsin proteins in-vitro, and were analyzed using the intensity-center algorithm implementation described above. However, the derivation of the simulation kymographs from discrete tracking data from the model system provided several advantages. Most notably, the structure of the tracking data, which included the association state of individual particles in the system as binary coordinates made it possible to generate discrete data describing the lifetime and persistence of individual particle-mobile unit interaction events and also allowed this data to be superimposed on the kymograph generated from the simulation constituting a powerful statistical and CGI correlate to tracking data generated for resolvable synapsin vectorial movements from kymographs generated from live imaging data, which are assumed to represent the specific interaction of synapsin particles with mobile-units via a mechanism similar to that enumerated in the above description of this model for synapsin transport.

SUPPLEMENTAL REFERENCES

Tsuriel, S., Geva, R., Zamorano, P., Dresbach, T., Boeckers, T., Gundelfinger, E.D., Garner, C.C., and Ziv, N.E. (2006). Local sharing as a predominant determinant of synaptic matrix molecular dynamics. *PLoS Biol* 4, e271.

Uchida, A., Alami, N.H., and Brown, A. (2009). Tight functional coupling of kinesin-1A and dynein motors in the bidirectional transport of neurofilaments. *Mol Biol Cell* 20, 4997-5006.

Wang, L., and Brown, A. (2002). Rapid movement of microtubules in axons. *Curr.Biol.* 12, 1496-1501.

Waterman-Storer, C.M., Desai, A., Bulinski, J.C., and Salmon, E.D. (1998). Fluorescent speckle microscopy, a method to visualize the dynamics of protein assemblies in living cells. *Curr Biol* 8, 1227-1230

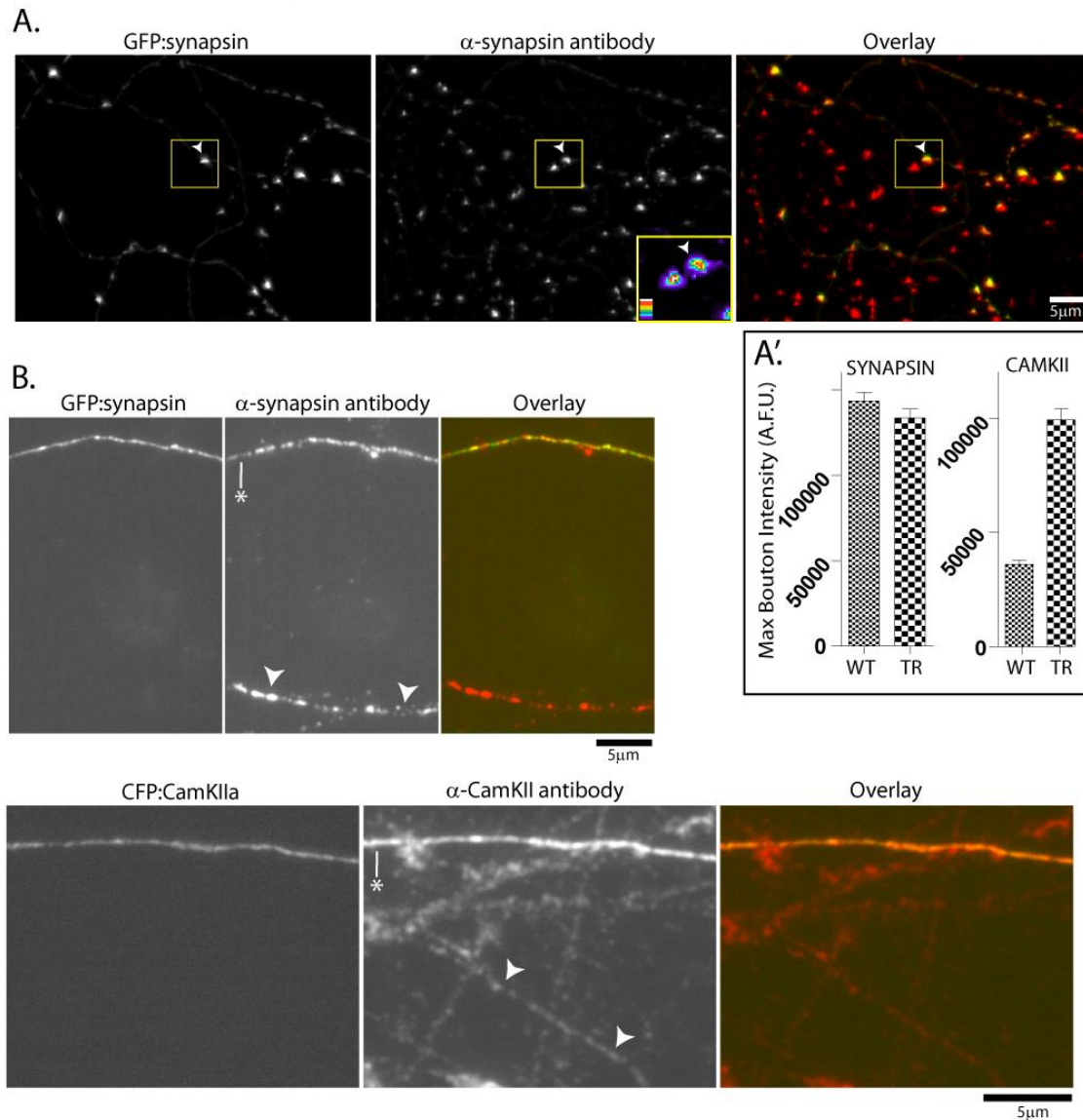


Figure S1. Characterization of the GFP-Fusion Proteins

DIV 7-10 hippocampal cultures were transfected with GFP:synapsin or GFP:CamKIIa, fixed after 24 or 48 hours respectively (maximum possible duration of over-expression in the imaging experiments), and then stained with antibodies to detect both transfected and endogenous proteins.

(A) Region containing boutons highlight the presynaptic targeting of the fusion protein. Adjacent transfected and un-transfected boutons are highlighted within the yellow box, arrowhead marks the transfected one. Note that relative protein levels within the two boutons are similar (see max-intensity 'heat-map' within magnified inset) for synapsin.

(A') Quantifications of un-transfected and transfected synapsin and CamKIIa boutons (N= 200-300 boutons for each group) are shown.

(B) Punctate synapsin and CamKIIa axonal particles were clearly observed in both transfected (marked with an asterisk) and un-transfected (marked with arrowheads) axons indicating that the expressed constructs appear to faithfully represent their endogenous counterparts.

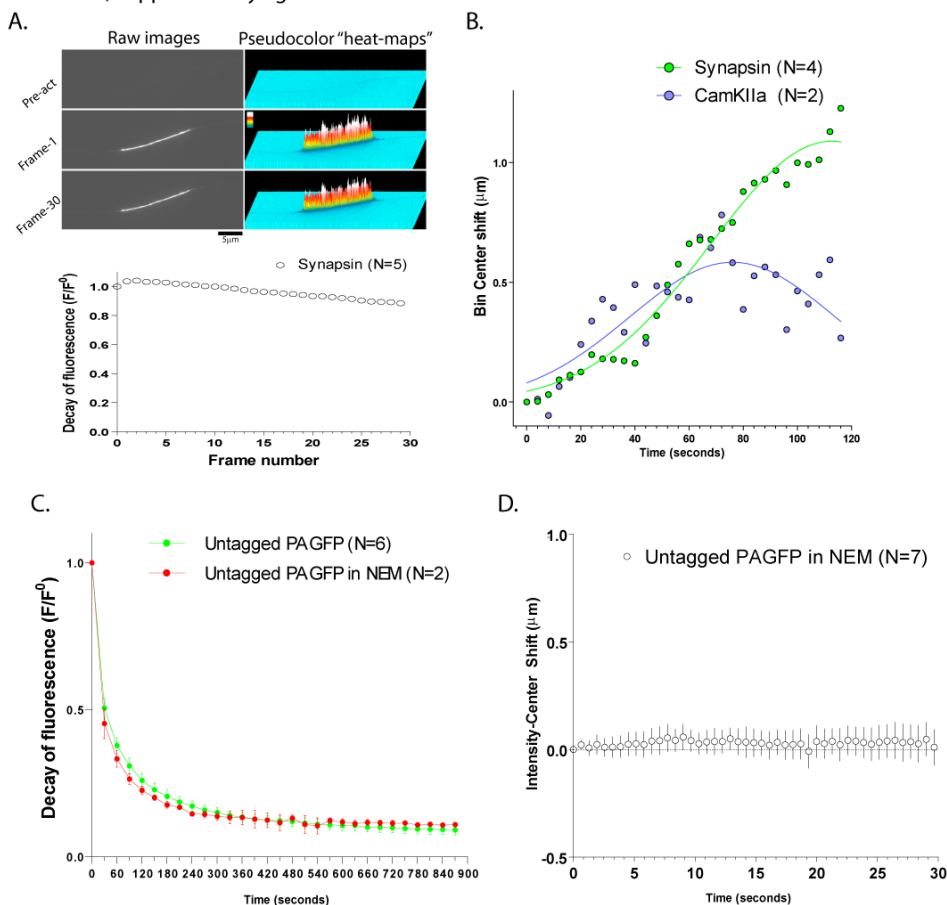


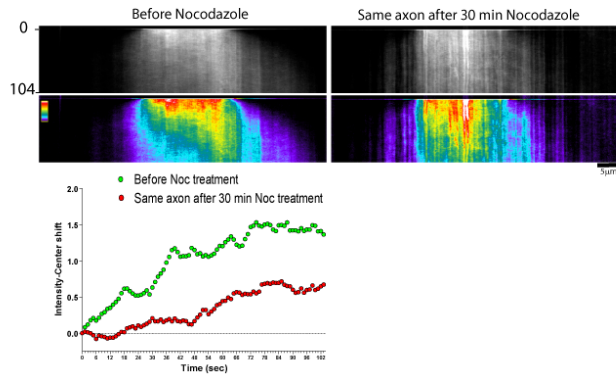
Figure S2. The Intensity-Center Shift of Synapsin and CamKIIa Is Not Influenced by Ongoing Photobleaching

(A) To determine imaging parameters with minimal ongoing photobleaching, neurons were co-transfected with PAGFP:synapsin and soluble mRFP (to identify transfected axons), fixed with 4% paraformaldehyde+120mM sucrose (37°C) for 10 minutes and then placed in the 'live-cell imaging' media (see methods for recipe). An axonal region was then selectively photoactivated and time-lapse images were obtained using our standard live-imaging parameters ($\approx 97\%$ reduction in light intensities, 1sec exposure; see methods for other parameters). The PAGFP within fixed axons could be readily photoactivated and we did not see any appreciable difference in the extent of photoactivation, as compared to living axons. To quantify photobleaching, we measured the fluorescence-decay of the photoactivated molecules within the fixed axon. As shown in the bottom graph, up-to 30 frames could be obtained using our specific imaging conditions with $<10\%$ loss in the overall intensity of the photoactivated zone.

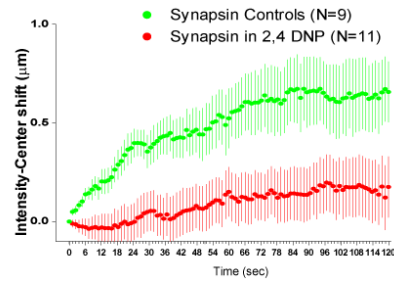
(B) Applying the above parameters, photoactivated axons containing PAGFP:synapsin and PAGFP:CamKIIa were imaged live (30 frames spanning 2 minutes, i.e. 1 frame/5 sec for 2 minutes) and the intensity-center shifts were determined (Gaussian fits shown). Note that the overall trend in intensity center shifts for these data are similar to that in Figure 2B, indicating that the intensity-center data are not significantly influenced by ongoing photobleaching. Scale bars: lower right.

(C and D) Neurons were transfected with untagged PAGFP, treated with NEM for 10 minutes and axons were photoactivated as described in the text. No differences were seen in either the decay-kinetics or the intensity-center shifts of the soluble protein under these conditions.

A. Effects of short-term nocodazole treatment on synapsin transport



B. Effects of 2,4 DNP on synapsin transport



C. Effects of headless Kinesins on synapsin and APP transport

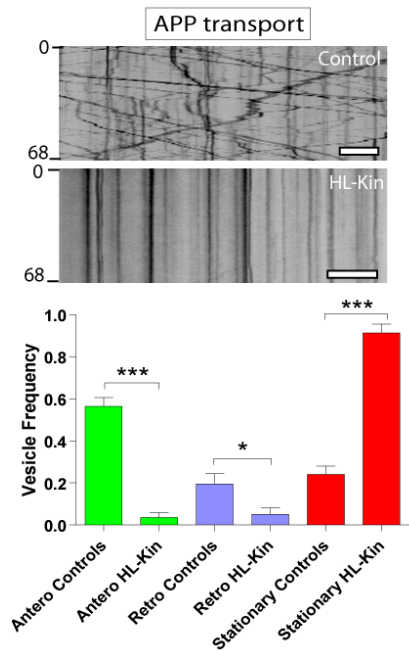
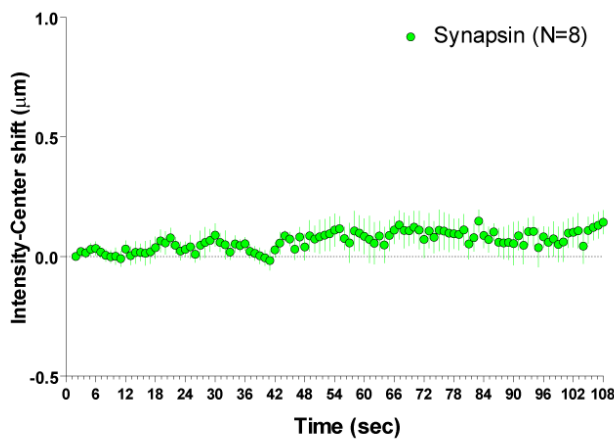


Figure S3

(A) Kymographs of the same axon before and after a 30 minute treatment with 10µg/ml Nocodazole clearly show an inhibition of anterograde bias and an increase in stalled particles within the axon.

(B) Neurons were treated with the metabolic inhibitor 2, 4DNP for 30 minutes and intensity-center shift was analyzed in living axons. Note the diminution of the anterograde bias upon 2,4 DNP treatment.

(C) Neurons were co-transfected with PAGFP-synapsin and a pool of dominant-negative headless Kinesin-1 (A/B/C) constructs; and axonal transport of synapsin was analyzed using the photoactivation paradigm after 17-24 hours. A marked diminution was seen in the anterograde bias of synapsin (mean ± SEM). As a positive control, the dominant negative Kinesin-1 constructs also caused a marked diminution in the transport of APP, a known Kinesin-1 cargo. Note that the bidirectional suppression of transport upon Kinesin-1 inhibition has been reported by many other studies (Uchida et al., 2009 for example), and may reflect physiologic interactions between Kinesin and Dynein cargoes (Scale bar: 5µm).

Particle-dynamics of SCb proteins revealed by “speckle imaging”

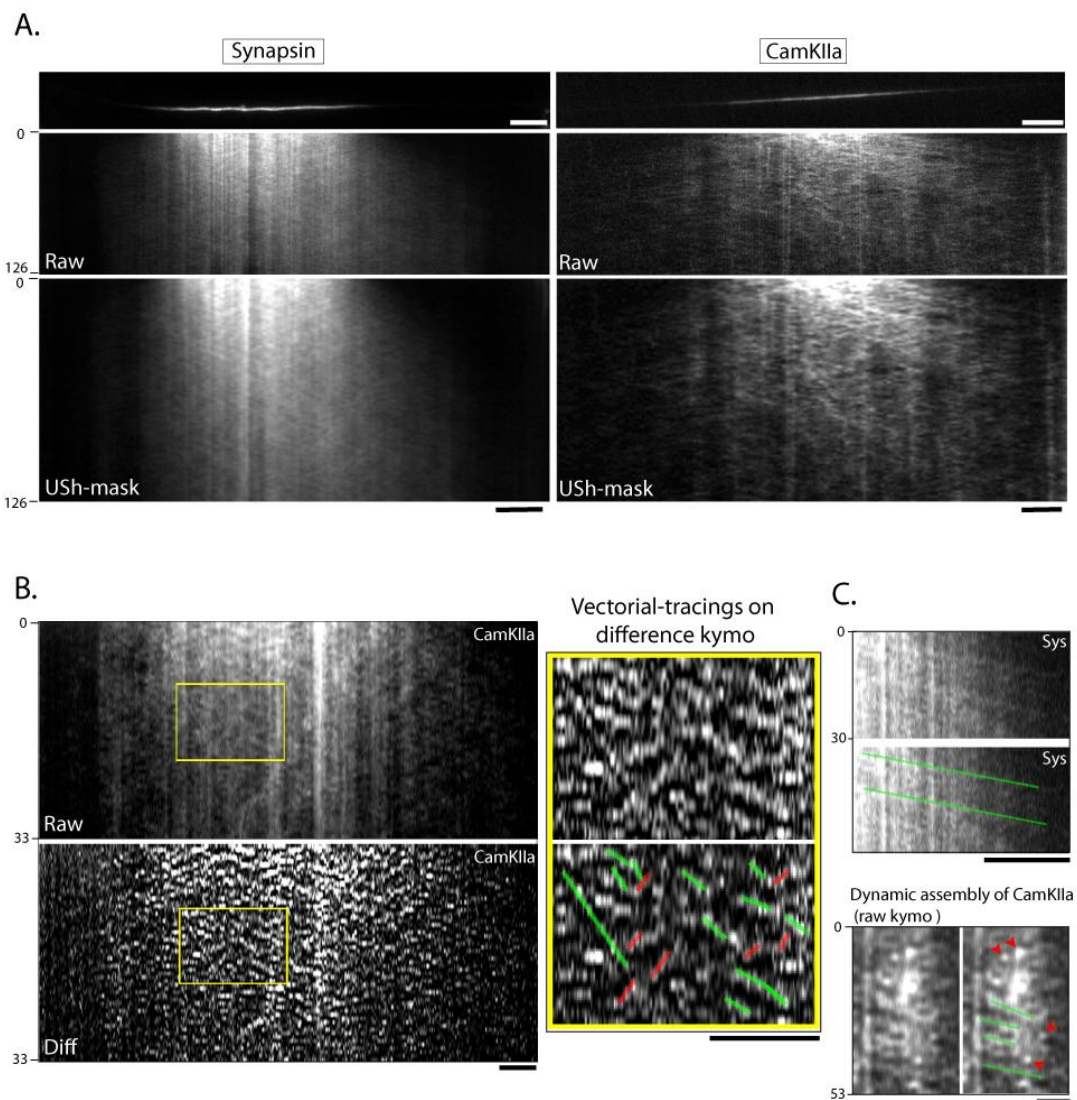


Figure S4. Particle Kinetics of Synapsin and CamKIIa.

(A) Axons expressing very low levels of PAGFP:synapsin and PAGFP:CamKIIa were photoactivated and imaged with high time-compressions as described in the text. Kymographs from raw (upper) and “unsharp-mask” (Waterman-Storer et al., 1998) movies obtained using these imaging parameters revealed an intricate bidirectional motion.

(B) The vectorial movements are highlighted by “difference-imaging” where the previous frame was subtracted to reveal vectorial particle motion (Wang and Brown, 2002). Note the intricate particle motion of CamKIIa (inset expanded on right, some anterograde/retrograde tracks are highlighted with red/green tracks respectively).

(C) Occasionally, persistent vectorial tracks (green overlaid lines) were observed as shown in the raw kymograph from a synapsin movie (top). Examples of appearance and disappearance of CamKIIa fluorescent speckles (red arrowheads) in addition to vectorial motion (green tracks) are shown in the bottom kymographs. Scale bars: 5 μ m, elapsed time in seconds: left of kymograph.

Scott et al., Supplementary fig. 5

Axonal transport imaging of APP after somatic photo-activation

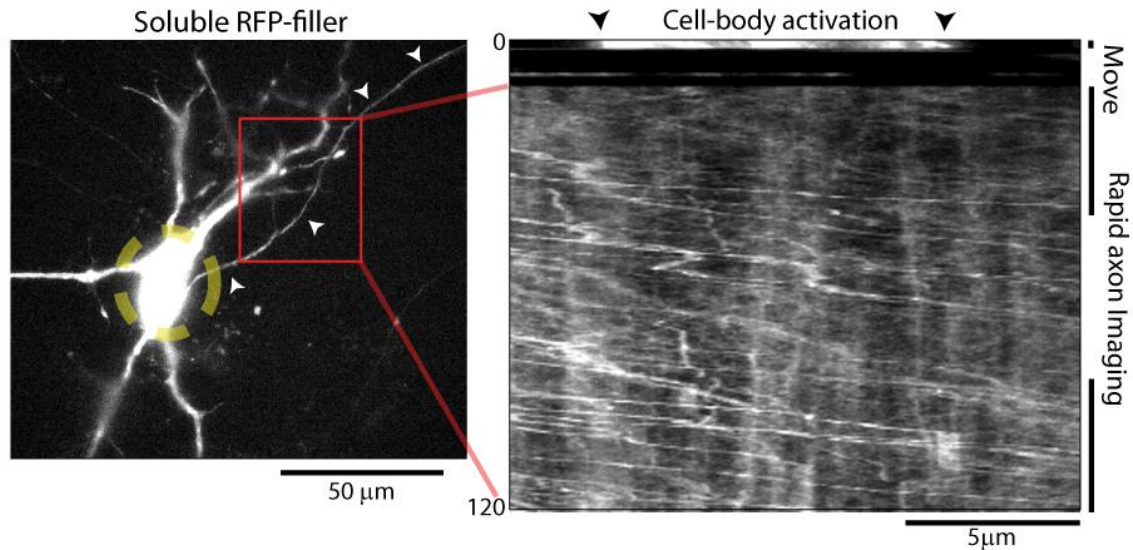


Figure S5. Visualization of Fast Axonal Transport Dynamics of Vesicles Originating in Cell Bodies.

Hippocampal neurons were transfected with APP:PAGFP, cell bodies were selectively photoactivated (region within dashed yellow circle) and transport of photoactivated APP vesicles was visualized in the emanating axon. To image the rapid transport of APP vesicles emerging from the cell body, after somatic photoactivation, the motorized stage was immediately moved to the proximal axon (within the red box) to image the emergent vesicles. Somatic-ly-derived photoactivated APP vesicles moved rapidly and persistently into the axon, with no slowly migrating wave as seen with synapsin. The kymograph on right shows the entire sequence of events- somatic photoactivation (between arrowheads), movement of the stage to the axonal ROI (≈ 10 sec), and the emergence of APP vesicles into the axon. Scale bars: lower right, elapsed time in seconds: left of kymograph.

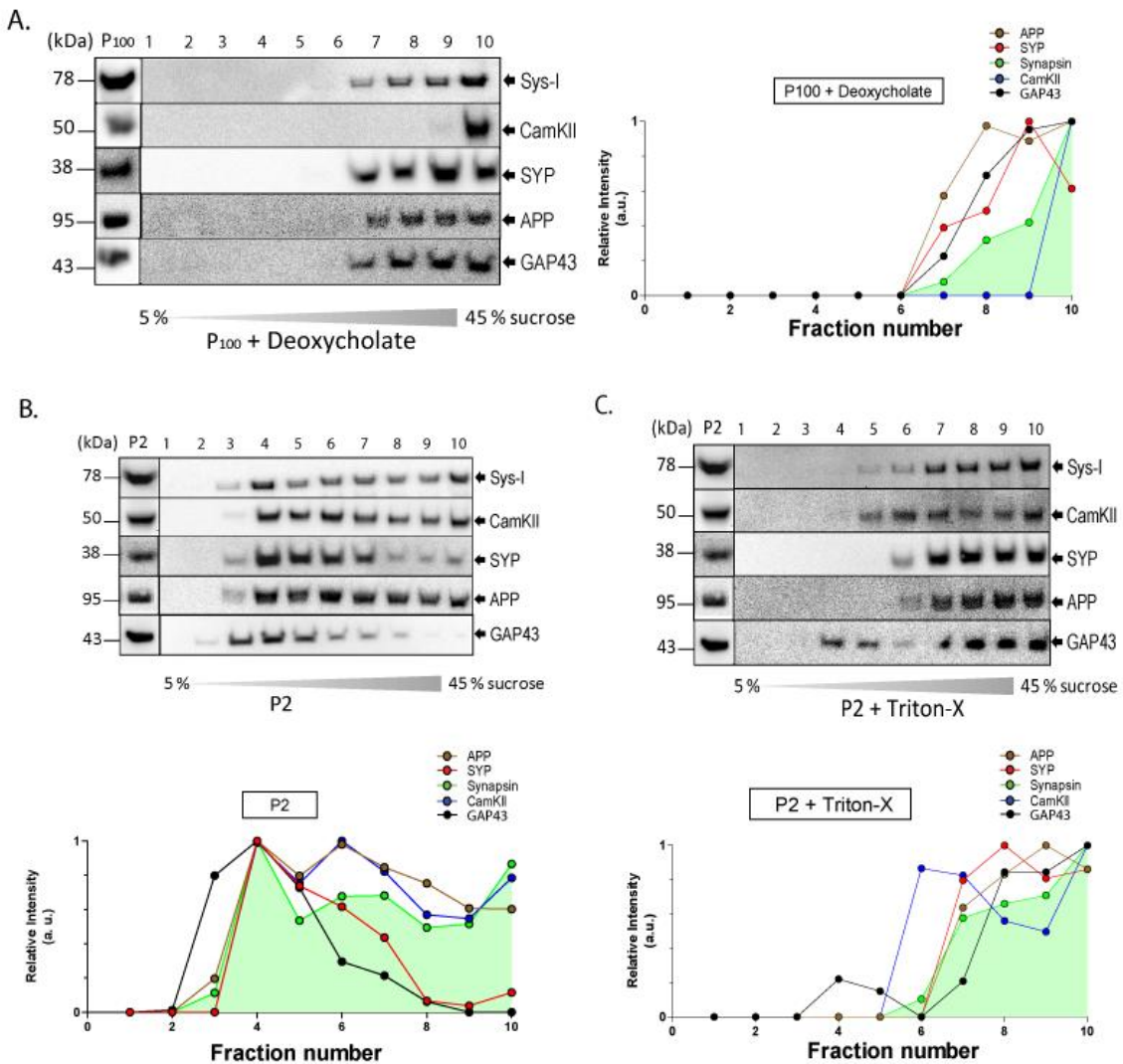


Figure S6. Additional Biochemical Analysis of Cytosolic Synaptic Cargoes

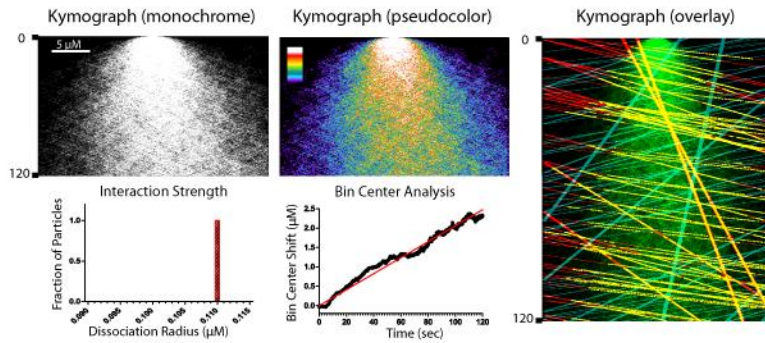
(A) Treatment with other membrane-disrupting detergents like deoxycholate led to similar results as with Triton-X, with disruptions in vesicular proteins and little effect on cytosolic cargoes, quantified by densitometry on right.

(B) In synaptosomal (P2) fractions, large proportions of synapsin and CamKII were also present in the lighter fractions.

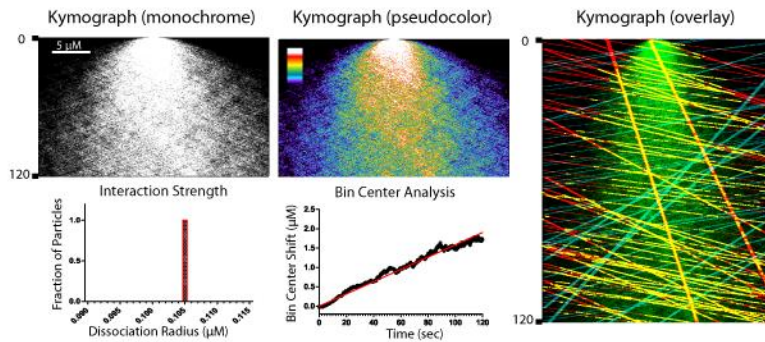
(C) Treatment of P2 fractions with 1% Triton disrupted the vesicular associations of the membrane-anchoring proteins synaptophysin, APP and GAP-43 as expected; as well as synapsin and CamKII pools present in the lighter fractions.

Scott et al., Supplementary figure 7

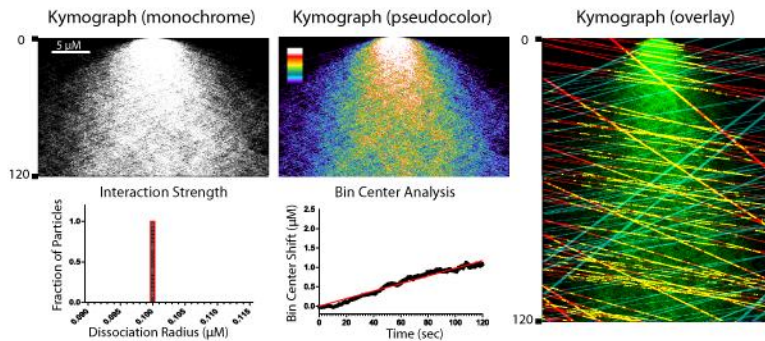
A. Modeling Dissociation Radius Constant: $0.110\mu\text{M}$



B. Modeling Dissociation Radius Constant: $0.105\mu\text{M}$



C. Modeling Dissociation Radius Constant: $0.100\mu\text{M}$



D. Modeling Dissociation Radius Constant: $0.095\mu\text{M}$

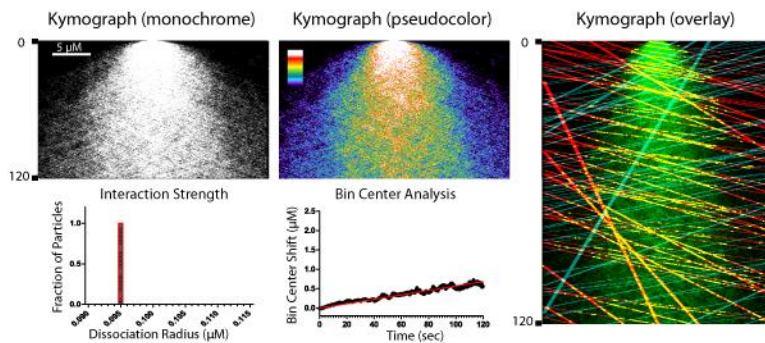


Figure S7. Introduction of Constant Association-Strengths in the Simulation Generated Continuously Linear Intensity Center Shifts.

(A-D) In the biophysical simulation, constant (invariable) interaction strengths were assumed between the synapsin particles and the mobile-units. Lower left graph shows individual numerical values for the interaction strengths and graph on lower right shows the intensity center shifts generated from each simulation. In the simulated multiple-parameter overlaid kymograph (middle) synapsin particles are shown in green and tracks of anterograde and retrograde mobile-units are depicted in red and blue respectively. The yellow tracks represent instances of colocalization of anterograde mobile unit tracks (red) and synapsin particles (green). Note that the reductions in interaction strengths (gradual decrease from top to bottom panels) led to diminutions of associations between synapsin particles and mobile-units and smaller virtual “run lengths” (note smaller colocalized tracks - yellow lines in the overlaid kymographs - from top to bottom panels).

Movie S1, Related to Figure 1A, Available Online. PAGFP:Synapsin Transport

Movie corresponding to the kymograph of PAGFP:synapsin axonal transport shown in Figure 1A; anterograde: left to right. Frames shown were acquired every 1.2 seconds for 59 seconds (time in minutes:seconds is shown on upper left). Vertical lines indicate the boundaries of the photoactivated zone. Arrowheads in the last frame indicate the leading and lagging “wave-fronts” of the mobile fluorescence pool. Note the anterograde bias of the mobile pool. Scale bar: 5 μ m, lower right. Images were acquired by wide-field epifluorescence microscopy coupled to a photoactivation set-up as described in the text.

Movie S2, Related to Figure 1B. PAGFP:CamKIIa Transport

Movie corresponding to the kymograph of PAGFP:CamKIIa axonal transport shown in Figure 1B; anterograde: left to right. Frames shown were acquired every 1.2 seconds for 61 seconds (time in minutes:seconds is shown on lower left). Vertical lines indicate the boundaries of the photoactivated zone. Note the anterograde bias of the mobile pool. Scale bar: 5 μ m, lower right. Images were acquired by wide-field epifluorescence microscopy coupled to a photoactivation set-up as described in the text.

Movie S3, Related to Figure 1C. Untagged Soluble PAGFP Transport

Movie corresponding to the untagged PAGFP kymograph shown in Figure 1C; anterograde: left to right. Frames shown were acquired every 2.4 seconds for 133 seconds. Elapsed time (of experiment) in seconds is shown on lower right. Note the rapid and unbiased departure of fluorescence from the photoactivated zone. Scale bar: 5 μ m. Images were acquired by wide-field epifluorescence microscopy coupled to a photoactivation set-up as described in the text.

Movie S4, Related to Figures 1D. PAGFP:APP Transport

Movie corresponding to the kymograph of APP:PAGFP axonal transport shown in Figure 1D; anterograde: left to right. Frames shown were acquired every 1.2 seconds for 31 seconds (time in minutes:seconds is shown on upper left). Small arrows indicate the boundaries of the photoactivated zone. Note the stochastic departure of fluorescent APP vesicles, distinct from the mobility of synapsin and CamKIIa. Scale bar: 5 μ m, lower right. Images were acquired by wide-field epifluorescence microscopy coupled to a photoactivation set-up as described in the text.

Movie S5, Related to Figure 2B. Untagged Soluble PAGFP:GFP Transport—High Time Compression

Example of untagged PA-GFP transport from the data-set in Figure 2B (lower right); anterograde: left to right. Frames shown were acquired every 0.3 seconds for 19 seconds. Small arrows indicate the boundaries of the photoactivated zone. Elapsed time (of experiment) in minutes:seconds is shown on upper left. Note that the elapsed time is deliberately slowed down in this movie to allow clear visualization of the unbiased rapid kinetics of untagged PAGFP within the axon. Images were acquired by wide-field epifluorescence microscopy coupled to a photoactivation set-up as described in the text.

Movie S6, Related to Figure 4A and Supplementary Figure 5. Somatic Exit of PAGFP:Synapsin

Movie corresponding to the kymograph(s) of PAGFP:synapsin axonal transport shown in Figure 4A(i); anterograde: left to right. The perikaryal PAGFP:synapsin was photoactivated and the mobility of the fluorescence in the emanating axon was imaged as described in the text. Frames shown were acquired every 5 seconds for over 8 minutes (time in minutes:seconds is shown on lower right). Note the slowly migrating fluorescence wave-front in the axon, best appreciated in the pseudocolor frames (second half of movie). Scale bar: 5 μ m, lower right. Images were acquired by wide-field epifluorescence microscopy coupled to a photoactivation set-up as described in the text.

Movie S7, Related to Supplementary Figure 5 and Figure 4A. Somatic Exit of PAGFP:APP

Movie corresponding to the kymograph(s) of APP:PAGFP axonal transport shown in Supplementary Figure 5; anterograde: left to right. The perikaryal APP:PAGFP was photoactivated and the mobility of the fluorescence in the emanating axon was imaged as described in the text. Frames shown were acquired every 1.2 seconds for over 3 minutes (over 10 minutes were imaged). Real elapsed time (of experiment) in minutes:seconds is shown on upper left. Note that to capture the initial exodus of photoactivated APP vesicles the field of view was shifted from the soma to the axon immediately after the photoactivation of the perikaryal APP, resulting in a few blurred images as the stage moved. Also note that numerous APP vesicles move with a strong anterograde bias, and no slow wave is observed, as seen with synapsin. Images were acquired by wide-field epifluorescence microscopy coupled to a photoactivation set-up as described in the text.

Movie S8, Related to Figure 6. Biophysical Simulation Model

Green particles in the central zone represent synapsin and the white spheres represent “mobile-units” (see text for details). At all times, synapsin particles were allowed to diffuse freely in a simulated aqueous cylinder (axon) according to known diffusion constants and also undergo collisions. Mobile-units were allowed to move in a vectorial manner across the simulated axon with velocities expected for motors/motor driven cargoes. Elapsed simulation time is shown on upper left.